frontiers | Frontiers in Astronomy and Space Sciences

TYPE Review
PUBLISHED 07 July 2025
DOI 10.3389/fspas.2024.1499346

OPEN ACCESS

EDITED BY
Shingo Kameda,
Rikkyo University, Japan

REVIEWED BY
Zhongwei Yang,
Chinese Academy of Sciences (CAS), China
Dolon Bhattacharyya,
University of Colorado Boulder, United States

*CORRESPONDENCE
Helmut Lammer,
helmut.lammer@oeaw.ac.at

RECEIVED 20 September 2024
ACCEPTED 19 November 2024
PUBLISHED 07 July 2025

CITATION
Lammer H, Schmid D, Volwerk M, Weichbold F, Wedlund CS, Varsani A and Delva M (2025) Ion cyclotron waves: a tool for characterizing neutral particle profiles in extended exospheres.
Front. Astron. Space Sci. 11:1499346.
doi: 10.3389/fspas.2024.1499346

Ion cyclotron waves: a tool for characterizing neutral particle profiles in extended exospheres

Helmut Lammer*, Daniel Schmid, Martin Volwerk, Fabian Weichbold, Cyril Simon Wedlund, Ali Varsani and Magda Delva

Austrian Academy of Sciences, Space Research Institute, Graz, Austria

Planetary exospheres are usually observed using transit spectroscopic methods, such as the Lyman-α line, which is mainly limited by interstellar medium absorption and airglow contamination from the geocorona when using low-orbit space telescopes or neutral and ion particle detectors and flight mass spectrometers. In this study, we discuss a complementary method that can be used for the characterization of exospheres based on the analysis of so-called ion cyclotron waves (ICWs) using magnetometers and plasma instruments. These ICWs are produced by pick-up ions from exospheric neutral atoms over a large spatial region upstream of planetary bodies. The newborn exospheric ions generate an unstable secondary ion population in the solar wind plasma, where the interaction between the exospheric and solar wind ion populations can produce plasma waves arising from various instabilities. The observed wave power can be used to derive the corresponding pick-up ion and related neutral particle densities. Because the ion pick-up density is balanced by the ion production rate, one can reconstruct the exospheric neutral number density. Various exospheric particles (i.e., H, H_2, D, He, etc.) can be distinguished by identifying their masses via their different gyrofrequencies even when they are very close to each other. In this study, we will discuss and analyze available ICW data as a tool for the reproduction of neutral atom profiles of extended exospheres, such as those of Mercury, Venus, Mars, the Jovian satellites, and comets.

KEYWORDS

ion cyclotron waves, exospheres, Mercury, Venus, Mars, icy satellites, comets

1 Introduction

Planetary exospheres are thin, collisionless, atmosphere-like gaseous envelopes surrounding planets or natural satellites, where atoms and molecules are gravitationally bound (Chamberlain, 1963; Bauer and Lammer, 2004). In the case of planets with atmospheres, such as Venus, Earth, or Mars, the exosphere is the layer above the thermosphere, where collisions become negligible and the gas thins out and can escape from the planetary body's gravitational field, extending into space. Atmosphere-less bodies, such as Mercury, the Moon, and Ceres, and icy satellites, such as Europa, Ganymede, or Callisto, have surface-bounded exospheres, which start at the surface of the object. In such cases, the surface material can be released into the surrounding environment through ion sputtering, photon- and electron-stimulated desorption, and evaporation caused by micrometeorite impacts so that exospheres consisting of surface material or externally

delivered material are formed (Wurz et al., 2022; Teolis et al., 2023). Ejected molecules move along elliptic trajectories, and when they remain neutral, these particles will collide with the planet's surface.

Smaller bodies such as asteroids, in which the molecules emitted from the surface escape to space, are not considered to have exospheres. Exospheres usually consist of atomic and molecular hydrogen (H, H_2) and helium (He) in their uppermost extended layers, with some heavier atoms and molecules near the exobase level that defines the transition from a collision-dominated regime near the exobase to the non-collision-dominated atmospheric region or to the surface in the case of airless bodies (Chamberlain, 1963; Bauer and Lammer, 2004; Lammer, 2013; Wurz et al., 2022). In an exosphere, the atoms and molecules are so distant that they can travel hundreds of kilometers without colliding with one another. Thus, the exosphere no longer behaves like a gas, and the particles with energies higher than the escape energy can be lost into space. There are four main methods used to study exospheres:

- Remote spectroscopic methods.
- Flight mass spectrometers and particle detectors onboard orbiting spacecraft.
- Solar wind charge-eXchange (SWCX) interaction analysis from ion analyzer data.
- Analysis of plasma and magnetic field observations by spacecraft, including ion cyclotron wave (ICW) analysis.

The first method by which exospheres of planets like Mercury, Venus, and Mars have been studied is the observation of resonant emission from excited atoms. Resonance emission takes place when solar photons of specific energies or wavelengths are absorbed and reemitted at the same wavelength. Because the combinations of energies at which such emissions occur vary between elements, the observed emission spectra provide spectral fingerprints for particular elements that populate the observed exosphere. As shown in Figure 1A, in 1974, the Mariner 10 spacecraft provided the first evidence that Mercury, the innermost planet of our solar system, is surrounded by a thin exosphere. The observed data with the UV spectrograph detected, for the first time, an abundance of exospheric H atoms through Lyman-α (121.567 nm) observations using the ultraviolet-visible spectrometer (UVVS) (Broadfoot et al., 1974), along with He at the 58.4-nm resonance line (Broadfoot et al., 1974; Hartle et al., 1975; Broadfoot et al., 1976).

During the mid-1980s, Potter and Morgan (1985) detected sodium (Na) from emission lines corresponding to the Fraunhofer sodium D lines in Mercury's exosphere, and 1 year later, potassium (K) was detected in its resonance line at 769.9 nm (Potter and Morgan, 1986) using a ground-based telescope and spectrometers. The variability in Mercury's Na exosphere was observed using the Time History of Events and Macroscale Interactions during Substorms (THEMIS) solar telescope (Leblanc et al., 2009). In July 1998, Bida et al. (2000) observed Ca in the planet's exosphere using the high-resolution Echelle spectrograph at the W. M. Keck I Telescope, focusing on the Ca line (422.674 nm).

In more recent times, the MErcury Surface, Space ENvironment, GEochemistry, and Ranging (MESSENGER) spacecraft observed Na (589.0 and 589.5 nm), Ca (422.7 nm), and H (121.6 nm) emissions (McClintock et al., 2008), and during its second and third flybys, the UVVS instrument also observed the Mg (285.2 nm) line (McClintock et al., 2009; Vervack et al., 2010). On 1st October 2021, the Probing of Hermean Exosphere by UV Spectroscopy (PHEBUS) instrument aboard BepiColombo (Benkhoff et al., 2021) observed He atoms during its first Mercury flyby (Quémerais et al., 2023), marking the first detection of He since the UVS measurements by Mariner 10 in 1974 (Broadfoot et al., 1974).

As shown in Figures 1B, C, extended atomic hydrogen exospheres were observed through Lyman-α dayglow emissions at several thousand km altitudes at Venus by Mariner 5 (Anderson and Donald, 1976; Cravens et al., 1980); these observations were later confirmed by Mariner 10 (Takacs et al., 1980), Venera 11 and 12 (Bertaux et al., 1978; 1982; Rodriguez et al., 1984; Lammer et al., 2006; Lichtenegger et al., 2006), Pioneer Venus Orbiter (PVO) (Paxton, 1985), and VEX (Chaufray et al., 2012), as well as Mariner 6 at Mars (Barth et al., 1969; Anderson et al., 1971). Suprathermal (hot) oxygen atoms that are dissociation products of molecular ions and products of charge exchange have also been detected in the exosphere at Mars and Venus for decades by various spacecraft such as the Mariner and Venera space probes, PVO (Nagy and Cravens, 1988), Mars Express (MEX), Mars Atmosphere and Volatile EvolutioN (MAVEN), the Emirates Mars Mission (EMM) probe, and VEX (Deighan et al., 2015; Jakosky et al., 2018; Holsclaw et al., 2021; Chirakkil et al., 2024). These atoms have been detected by detecting resonance fluorescence emissions at 130.4 nm. The Emirates Mars Ultraviolet Spectrometer (EMUS) instrument onboard the EMM spacecraft (Holsclaw et al., 2021) indicated that the emission of the OI 130.4 nm is highly correlated with solar irradiance and changes in the Sun–Mars distance.

One of the main goals for observing particles in exospheres whose densities can then be reproduced by upper atmosphere models is the determination of accurate atmospheric escape rates. Due to Venus being ≈7.6 times more massive than Mars, Jean's escape of neutral H atoms at a rate of $\approx 2.5 \times 10^{19}$ s^{-1} is negligible compared to the rate of $\approx 1.5 \times 10^{26}$ s^{-1} at the smaller planet. H atoms that are lost with rates of $\approx 3.8 \times 10^{25}$ s^{-1} from Venus' exosphere belong to suprathermal H atoms that are produced via photochemical reactions (Lammer et al., 2006). From MAVEN observations, an average escape rate of suprathermal O atoms from Mars' exosphere is $\approx 5 \times 10^{25}$ s^{-1} (Jakosky et al., 2018), while the direct escape of these heavy neutral atoms from Venus' exosphere is negligible (Lammer et al., 2006).

The ionized fraction of planetary exospheres is mainly detected and characterized through measurements obtained from flight mass spectrometers and particle detectors. The first flight mass spectrometer measurements in Mars' exosphere were carried out using the Automatic Space Plasma Experiment with a Rotating Analyzer (ASPERA) at the planet's magnetic boundary (Lundin et al., 1989; Rosenbauer et al., 1989) onboard the Phobos 2 spacecraft. The ASPERA instrument package was designed to study the solar wind interaction with the Martian upper atmosphere so that the plasma and neutral particle environment could be characterized, locally charged particles could be measured, and energetic neutral atoms (ENAs) could be imaged. Measurements were carried out using ENA sensors and ion and electron spectrometers (Barabash et al., 2004), where the neutral particle imager (NPI) measures ENA fluxes within an energy resolution range of ≈0.1–10 keV and the ion mass analyzer (IMA) measures ions in the energy range of ≈0.01–40 keV per charge for ion

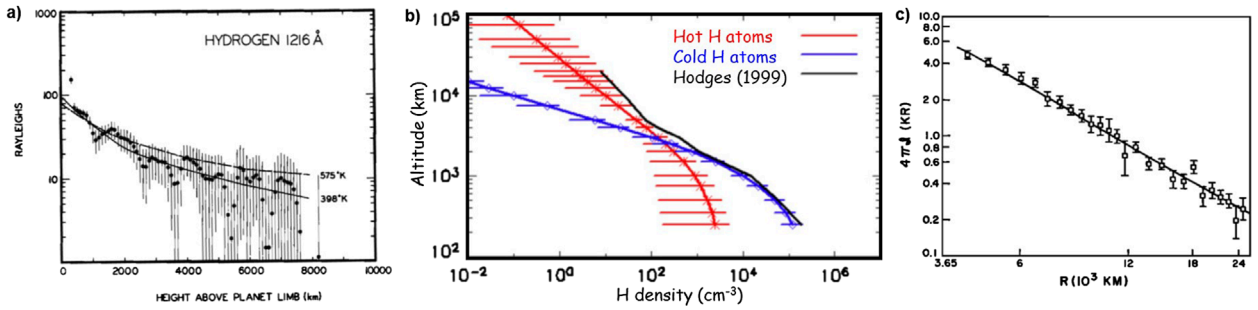

FIGURE 1
Exosphere profiles derived from Lyman-α observations at Mercury, Venus, and Mars. Panel **(A)**: Observations of the atomic hydrogen corona above the subsolar point during Mercury flyby by Mariner 10 (Broadfoot et al., 1976). Panel **(B)**: Average, thermal (cold), and suprathermal (hot) atomic H densities in Venus' exosphere near noon, compared to the modeled H density profile presented by Hodges (1999). The horizontal lines correspond to the variability derived from Lyman-α observations by SPICAV onboard Venus Express (VEX) (Chaufray et al., 2012). Panel **(C)**: Best fit to the Mariner 6 data for Mars including radiative transfer effects with the Lyman-α intensity modeled and shown with the solid line (Anderson et al., 1971).

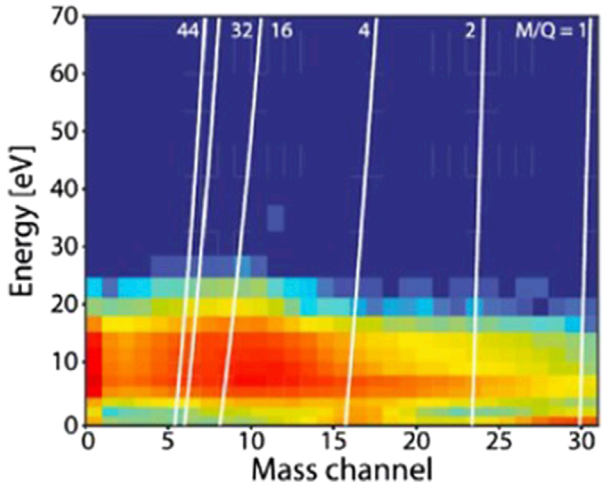

FIGURE 2
ASPERA-4/IMA mass spectrogram data during a pericenter pass of Venus Express at Venus on 2 July 2014. The white lines indicate the mass per charge of ions obtained from ground calibrations. IMA was not sensitive enough to separate exospheric H^+ ions from D^+ or H_2^+ ions (Persson et al., 2019).

components (H^+, He^+, He^{++}, and O^+) (Barabash et al., 2004). During the Phobos 2 mission, the ASPERA instrument observed exospheric hydrogen ions, O^+ ions, and O_2^+ ions that were used for the reconstruction of ion escape rates and exospheric ion densities (Lundin et al., 1990; Lundin et al., 2007). More detailed studies on the ion part of the exospheres of Mars and Venus were carried out using the follow-up instruments ASPERA-3 and ASPERA-4 (Lundin et al., 2006; Lundin et al., 2007). However, as shown in Figure 2, it should be noted that it was not possible to separate exospheric H^+ pick-up ions from H_2^+ or D^+ ions using the follow-up IMA of ASPERA-3 and ASPERA-4 onboard Mars Express and Venus Express.

Figure 2 shows an IMA energy–mass spectrogram of ions at Venus, where the masses per charge are smeared over the mass channels so that one cannot separate small mass differences (Persson et al., 2019). It should be noted that both instruments also have an integrated 'neutral particle detector' (NPD) that measures ENAs that originate via charge exchange with solar wind protons and exospheric H atoms (Lichtenegger et al., 2006; Galli et al., 2008; Lammer et al., 2006). After analyzing MEX ASPERA-3 and MAVEN data, the escape of exospheric O^+ ions on Mars was found to be between $\approx 1.6 \times 10^{23}$ s^{-1} (Barabash et al., 2007) and $\approx 5.0 \times 10^{24}$ s^{-1} (Jakosky et al., 2018). By analyzing all VEX ASPERA-4 measurements, it was found that H^+ ion escape varies from 7.6×10^{24} s^{-1} at the solar minimum to $\approx 2.1 \times 10^{24}$ s^{-1} at the solar maximum, while the O^+ escape rate exhibits a smaller variation from $\approx 3 \times 10^{24}$ O^+ s^{-1} at the solar minimum to $\approx 2.0 \times 10^{24}$ O^+ s^{-1} at the solar maximum (Persson et al., 2018).

A further example of exospheric particle detectors is the so-called Search for Exospheric Refilling and Emitted Natural Abundances (SERENA) instrument, which is onboard BepiColombo's MPO spacecraft (Benkhoff et al., 2021). The SERENA instrument package consists of two complementary neutral and two ion particle detectors (Orsini et al., 2021), where the STart from a ROtating Field mass spectrOmeter (STROFIO) measures *in situ* the low-energy neutral particle composition and density in the energy range $<$ 1 eV and the Emitted Low-Energy Neutral Atoms (ELENA) instrument covers the higher-energy spectrum between 20 eV and 5 keV of neutral particles. The two remaining detectors are the miniature ion precipitation analyzer (MIPA), which monitors the solar wind plasma flow between 15 eV and 15 keV, and the Planetary Ion CAMera (PICAM), which is optimized to measure low-energy planetary ions up to 3 keV with a higher mass resolution than MIPA. After BepiColombo reaches Mercury's orbit, the SERENA instrument package will provide information that can be used for the characterization of the whole coupled surface–exosphere–magnetosphere environment; this includes the study of various physical processes, including the interactions between the solar wind and energetic particles, and effects of micrometeorite delivery, impact evaporation, and the processes occurring in the interplanetary space (Orsini et al., 2021).

A third technique to derive the density and characterize the exosphere environment of a planetary body is illustrated in Figure 3.

In this approach, the exosphere density and outflow rates of the studied target are inferred through a detailed analysis of charge-transfer processes, known as SWCX interaction analysis, between energetic solar wind or exospheric ions and exospheric neutrals. An advantage of this technique is that it does not necessarily need a mass spectrometer onboard the spacecraft. Simon Wedlund et al. (2016); Simon Wedlund et al. (2019a); and Simon Wedlund et al. (2019b) applied this method for the first time to characterize the composition of the dayside neutral coma of the comet 67P/Churyumov–Gerasimenko. The Rosetta Plasma Consortium Ion Composition Analyzer (RPC-ICA) measured theHe^{+}/He^{++} flux ratios, which are easily distinguishable by their energy per charge in the data. The abovementioned authors applied exospheric densities and analyzed the charge-exchange processes between the solar wind and cometary neutrals until the observations of theHe^{+}/He^{++} flux ratios could be reproduced. After reproducing the coma density with this technique, neutral H_2O outgassing rates in heliocentric distances for comet 67P/Churyumov–Gerasimenko between 1.8–3.3 AU of $\approx 1.0 \times 10^{27}$ s^{-1}–$\approx 2.2 \times 10^{25}$ s^{-1} were found. Halekas (2017) analyzed SWCX data obtained from the MAVEN solar wind ion analyzer (SWIA) (Halekas et al., 2015) with support from the spacecraft's SupraThermal And Thermal Ion Composition (STATIC) (mass spectrometer) instrument and derived the column density of exospheric H atoms upstream of Mars' bow shock. By applying various Chamberlain-type model exosphere profiles, Halekas (2017) constrained the profile and escape rates of exospheric H atoms with this technique. Follow-up studies with the SWCX technique indicate that Mars' atomic hydrogen exosphere and escape rates are highly sensitive to seasonal variability and solar activity (Halekas and McFadden, 2021). It is important to note that this exosphere characterization method is also complementary to the other briefly discussed methods and should also be applied to Venus' exosphere in the near future.

A fourth method, which has not been used so often to characterize planetary exospheres—especially their extended regions—is related to plasma physics and *in situ* magnetic field observations. Various spacecraft such as Galileo (Jupiter system), MEX (Mars; but no magnetometer data), VEX (Venus), MESSENGER (Mercury), and BepiColombo (Mercury) had/have plasma and magnetometers embarked that can detect so-called electromagnetic ICWs. ICWs are generated by temperature anisotropy in plasma that is embedded in a background magnetic field, where the perpendicular temperature is larger than the parallel temperature (Gary, 1991). In a planetary environment, such anisotropy can be obtained by picking up freshly ionized exospheric neutral particles by the background magnetic field. As exospheric neutral atoms become photo-ionized, they start gyrating around the background interplanetary magnetic field (IMF) and get picked up by the solar wind plasma flow. Because the velocity of the newly generated planetary ions is of the order of a couple of km/s, which is very different from the solar wind velocity that reaches hundreds of km/s, the solar wind plasma becomes unstable to different plasma waves via resonant and non-resonant instabilities (Gary, 1991). This instability mechanism has already been shown to take place in any planetary environment with a spatially extended exosphere, such as the Jovian satellites Europa (Volwerk et al., 2001) and Io (Russell et al., 2003; Russell and Blancocano, 2007), Mercury (Schmid et al., 2022; Schmid et al., 2025; Weichbold, 2023; Weichbold et al. 2025), Venus (Russell and Blancocano, 2007; Delva et al., 2008a; Delva et al., 2008b; Delva et al., 2011; Wei et al., 2011), Mars (Russell et al., 1990; Mazelle et al., 2004; Russell and Blancocano, 2007; Delva et al., 2011), and comets (Huddleston et al., 1992a; Huddleston et al., 1992b; Volwerk et al., 2013a; Volwerk et al., 2013b). From the observed wave power of detected ICWs, the photoionization rate, and the ion production rate, one can derive the local density of the corresponding neutral particles, and thus, the related density profiles of the extended exosphere can be reconstructed. Depending on the magnetic field strengths, the gyro radius of the ionized exospheric particles, elements from masses between 1–7 amu, have been detected and analyzed in the space environment around Mercury, Venus, Earth, and Mars; moreover, ICWs have been detected from water-group ions over the E-ring of Saturn and near comets 27P/Grigg–Skjellerup and 1P/Halley. Compared to the previously mentioned exosphere characterization methods, we point out that the ICW technique is advantageous mainly for the following points:

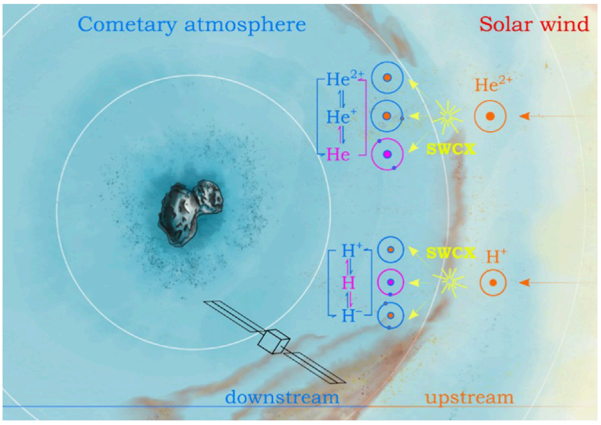

FIGURE 3
Illustration of solar wind charge exchange interaction processes near the environment of comet 67P/Churyumov–Gerasimenko at approximately 2 AU. The upstream solar wind H^{+} and He^{++} ions interact during charge-exchange processes with the cometary neutral atmosphere–exosphere, which is shown in an increasingly deep blue color. The interactions illustrated in yellow produce charged states in the downstream region of the collisions. Energetic neutral atoms are shown in pink. The red shaded areas correspond to the heated and deflected solar wind around the bow-shock-like structure, where SWCX plays a major role (Simon Wedlund et al., 2019b).

- It is sensitive to very low exospheric number densities and, therefore, is ideally suited for determining exosphere densities in the outer layers of the exosphere.
- It can be used to analyze and separate thermal exospheric particle populations from non-thermal particles (i.e., micrometeorite impact evaporation, sputtering on airless bodies such as Mercury and the Moon, or suprathermal particles in the extended exospheres of Venus, Mars, Earth, etc.).
- It is a technique that is sensitive enough to separate atomic hydrogen from molecular hydrogen, or in the case of Venus, it should be possible to separate suprathermal H atoms from D isotopes.

Although ICWs and related magnetic field data have been studied on various planetary bodies, ICW-related data have only been roughly applied for the characterization of the composition and density of planetary exospheres. This review addresses strengths and future applications of this method. In the following sections, we will focus on the observations and the method where ICWs can be used to reproduce densities of various species in extended exosphere layers, with a focus on Mercury and Venus. We also review and discuss observations of ICWs on Earth, Mars, icy satellites, and comets. In Section 2, we describe the necessary data and parameters that are needed for the analysis of ICWs generated by exospheric pick-up ions. We also emphasize how one can use plasma and magnetic field measurements for the detection of exospheric species that cannot be detected by spectroscopic techniques or particle detectors and how ICW analysis serves as a helpful complementary method to the other techniques mentioned above. Moreover, we describe in detail the technique to retrieve the exospheric neutral density profiles from ICW data. In Section 3, we present and discuss exospheric neutral density profiles of various species derived from the analysis of ICWs at Mercury and Venus. Moreover, we also provide a brief review of available ICW observations in the exosphere environments of Earth, Mars, icy satellites, and comets and how these data can be used to characterize their exospheres in the near future. Section 3 will be completed with an outlook on how future ICW observations at the Jovian satellites by the JUICE mission (Grasset et al., 2013) and on a cometary target studied by the Comet Interceptor (Jones et al., 2024) mission can be complementarily used with mass spectrometers for the characterization of their neutral and ionized exosphere environments. Section 4 provides the conclusion of this work.

2 ICW analysis and retrieval of particle densities in extended exospheres

In space plasma physics, ICWs are longitudinal oscillations of ions and electrons in a magnetized plasma that propagate nearly perpendicular to the magnetic field. The newborn ions are picked up by the IMF, which usually has an angle α_{BV} with the direction of the solar wind velocity. Depending on this angle, the pick-up distribution can vary from a ring distribution for $\alpha_{BV} = 90°$ to a beam distribution for $\alpha_{BV} = 0°$, but the distribution is usually a combination of the two: ring–beam distribution. In the case of a ring distribution, there are two competing instabilities, the ICW and the mirror mode instability, where the dominant mode is determined by the plasma-β. The ICWs arise from the ion–ion LH instability, leading to a parallel-propagating wave LH mode in the plasma frame. In the case of a beam-distribution, the ion–ion RH instability occurs, which generates a wave with the maximum growth rate in the parallel direction to B (Gary, 1991; Huddleston et al., 1992a; Huddleston et al., 1992b). Most often, we have a ring–beam distribution for all intermediate cases of α_{BV}.

In planetary environments, besides the interplanetary magnetic field (IMF), magnetic fields can be intrinsically generated by a magnetic dynamo or induced due to the interaction between a planetary body and the solar wind. In the latter case, the solar wind interaction leads to a bow shock and an induced magnetospheric obstacle close to the planet. In the case of Mercury, Venus, Mars, icy satellites, comets, etc., a substantial part of the upper neutral exosphere is outside the magnetic obstacle and upstream of the bow shock and is, therefore, directly accessible to the solar wind plasma flow (Luhmann and Bauer, 1992). A fraction of the exospheric neutral particles will then be ionized by mainly photoionization, electron impact ionization, and charge exchange. These newborn exospheric ions produce a planetary ion population in the solar wind, where its interaction with the plasma background enables the generation of electromagnetic waves at the ion cyclotron frequency. The produced ICWs can be expected at any location where the pick-up of ionized exospheric neutrals is possible, especially in the extended exosphere regions and upstream of the bow shock (Delva et al., 2008a; Delva et al., 2008b). Unlike plasma waves caused by backward-flowing solar wind ions located in the foreshock region defined by magnetic field lines tangential to the bow shock, ICWs occur anywhere upstream of the environment (Mazelle et al., 2004). In addition, their frequencies are very different, and those backstreaming ions have much lower frequencies than the local IC frequency. Because of this, the observation of ICWs in the upstream region of a planetary body confirms that certain exospheric ions are present and are being carried away by the solar wind into interplanetary space.

Figure 4 shows a schematic illustration of the generation of ICWs around a planetary environment. Neutral exosphere particles (gray dots: 1) are ionized due to photons, electron impact, and charge exchange (purple lines: 2); then, the newborn solar wind picks up exospheric ions and starts to gyrate around the IMF (green lines: 3). By using the solar wind frame as a reference, the exospheric pick-up ions form a secondary distribution in the velocity space that is highly unstable to the cyclotron wave instability, and ICWs (orange lines: 4) are excited. As illustrated in Figure 3, ICWs are mainly generated by pick-up ions upstream of the bow shock with a specific frequency and polarization in the spacecraft frame. The angle between the bulk velocity of the solar wind and the magnetic field vector determines the mechanism for the generation of the ICWs via the growth rate of unstable modes. For perpendicular conditions between the solar wind bulk velocity and the magnetic field, the newly born exospheric ions form a ring-like distribution in velocity space, with the free energy acting as a source for ICWs (Coates et al., 1990; Volwerk et al., 2001; Bertucci et al., 2005; Delva et al., 2008a; Delva et al., 2008b; Delva et al., 2011; Delva et al., 2015).

For quasi-parallel or antiparallel conditions between the solar wind bulk velocity and the magnetic field, newly born ions form a field-aligned beam of exospheric ions, where the free energy given in Equation 1, determined by Huddleston and Johnstone (1992) is as follows:

$$E_{free} = 0.25\,\phi\, m_i\, n_i\, v_A\, v_{inj}\left\{[1+\cos(\alpha)]^2 + [1-\cos(\alpha)]^2\right\}, \quad (1)$$

which is carried in the parallel drift velocity of the ions relative to the background plasma (Gary, 1991; Gary and Winske, 1993). Here, v_A and v_{inj} are the Alfvén and the plasma injection velocities, respectively, and α is the pitch angle between the background magnetic field and v_{inj}. If one assumes a complete scattering of the ring-like distribution, then the so-called energy transfer efficiency ϕ would be 1. In such a case, the energy in the waves is equal to the free energy. According to 1D hybrid simulations by Cowee et al. (2007), the efficiency of converting particle to wave power is not 100% but ≈30%.

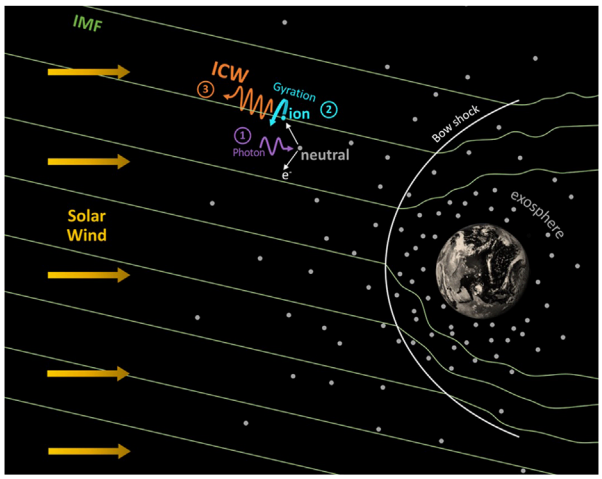

FIGURE 4
Illustration of the ion cyclotron waves generation mechanism near planetary environments. Exospheric neutral atoms get ionized (gray dots) by solar photons (1: purple line). Newborn ions (2: blue) begin to gyrate around the IMF lines and get picked up by the solar wind plasma flow. In the solar wind frame of reference, these picked up ions from a secondary distribution in the velocity space that is highly unstable to the cyclotron wave instability and ICWs (3: orange line) are excited (Schmid et al., 2022).

To determine the ion pick-up-related ICWs in the magnetic field, the data are split into intervals that can be described as sliding windows; within every interval, the data will be transformed into the mean field-aligned coordinate system (Schmid et al., 2021; Schmid et al., 2022; Weichbold, 2023; Weichbold et al., 2025). These intervals are separated into subintervals, and a fast Fourier transformation and a 'power spectral density' (PSD) analysis are then performed (Means, 1972; Samson and Olson, 1980), where further properties of the waves, such as ellipticity and the wave vector, are determined by the off-diagonal elements of the PSD matrix. The calculated values of the subintervals are averaged, and specific selection criteria based on the picked up ions' characteristics for ICWs can be applied. By fulfilling this selection criterion, the fluctuations within this interval are then identified as pick-up ion-based ICWs. Since the gyrofrequency of the picked up ions is given by the charge of the ion multiplied by the inverse of the particle mass and the total magnetic field strength, it is possible to distinguish between different exospheric pick-up ion species. The specific frequency of ICWs in the spacecraft frame enables a clear distinction between plasma waves that are generated by exospheric ions and those that belong to solar wind protons. Waves that are produced by solar wind protons that are reflected by the bow shock are observed with a much lower frequency than ICWs that originate from exospheric ions and are limited to the foreshock region (Shan et al., 2014).

One can analyze the ICWs that are generated by picked up ions using solar wind and plasma data such as solar wind velocity and density (Fränz et al., 2017; Rojas Mata et al., 2022). The pick-up ion number density n_i is balanced by the ion production rate, and the neutral particle number density of the exospheric particle can, therefore, be determined using (Schmid et al., 2022; Weichbold, 2023; Weichbold et al., 2025) the following equation:

$$n_n = \frac{2\pi n_i f_{c,i}}{100\nu}, \tag{2}$$

where ν is the photoionization rate at the location of the planetary body and the pick-up number density is represented by n_i, and the gyrofrequency shown in Equation 3 of the exospheric pick-up ions is given by

$$f_{c,i} = \frac{qB}{2\pi m_i}, \tag{3}$$

with the electric charge q, the magnetic flux density B, and the mass of the exospheric pick-up ion m_i. The choice of 100 gyro-periods until the ICWs reach their full development and attain a quasi-steady state, as proposed by Schmid et al. (2022); Schmid et al. (2025) and Weichbold (2023), can certainly be considered conservative and is based on one-dimensional hybrid model simulations at sub-Alfvénic pick-up ion velocities, indicating that a complete energy transfer from ions to waves occurs over ≈60 – 100 ion gyrations (Cowee and Gary, 2012; Cowee et al., 2012). The results from hybrid model simulations indicate that ICWs grow until a quasi-steady level is reached after several tens of ion gyrations.

The waves will be observed at the local ion gyrofrequency in the spacecraft frame and with specific left-hand polarization due to the anomalous Doppler effect (Mazelle and Neubauer, 1993). This fact immediately excludes confusion with ULF waves generated by solar wind protons back-streaming from the bow shock, which will be observed at the spacecraft at frequencies much lower than the cyclotron frequency (Gary, 1991) and occur only within the foreshock.

Moreover, it is important to note that one can distinguish ICWs from exospheric particles with masses that lie close together, such as atomic and molecular hydrogen or H atoms and D isotopes. In this context, as shown in Figure 2, it was not possible to separate H^+ ions from H_2^+ or D^+ ions using the ion mass composition sensor (IMA) of ASPERA-4 onboard Venus Express (Persson et al., 2019) because the mass-per-charges are very smeared over the mass channels. Since H_2 molecules that have a similar mass to D do not populate the Venus exosphere (Taylor et al., 1985; Hodges, 1999) and the ICW method is crucial to the local gyrofrequency $f_{c,i}$, one can separate ICWs between H^+ and D^+ so that this method is the only one that can be used for the detection and reproduction of exospheric D profiles at Venus.

For the analysis of ICWs, the following identification criteria can be defined (Schmid et al., 2022) after one has identified ICW events in the space environment around a planetary body. To identify the pick-up produced ICWs, one can use magnetic field observations of approximately 20 Hz applied to the following steps within a sliding interval that lasts ≈100s (Schmid et al., 2021; Schmid et al., 2022):

- Magnetic field data are transformed into a mean-field-aligned (MFA) coordinate system.
- Fourier-transformed ≈30 subintervals for light elements (i.e., H, H_2, and He) of the magnetic field data with ≈50% overlap are formed, and the power spectral density matrix is evaluated.
- The diagonal elements of the power spectral density matrix represent the parallel and perpendicular in-phase power densities relative to the mean magnetic field. The ellipticity and the handedness of the observed electromagnetic wave are inferred from the complex off-diagonal elements to

the power spectral density matrix, where negative/positive signs refer to the left/right-handed polarization of the wave in the spacecraft frame (Arthur et al., 1976; Samson and Olson, 1980; Schmid et al., 2022).
- The polarization degree of each subinterval is determined.

Considering the aforementioned steps, the arithmetic means of the ellipticities and power densities of the subintervals are calculated. Another condition for ICWs that are produced by exospheric pick-up ions is that the observed frequency in the spacecraft frame is close to the local ion gyrofrequency $f_{c,i}$ (Delva et al., 2008a; Schmid et al., 2022). By applying the criteria in the frequency range (Schmid et al., 2022), we obtain

$$\Delta f = \left[0.8\left(f_{c,i} - \Delta f_{c,i}\right), f_{c,i} + \Delta f_{c,i}\right], \quad (4)$$

where $\Delta f_{c,i}$ is the error range within the average and standard deviation of the gyrofrequency. For each of the 100 s time intervals, the following additional criteria can be introduced (Schmid et al., 2022):

- To account for a power maxima below the $f_{c,i}$, the power density per component is integrated within the frequency range Δf as given in Equation 4.
- Within the frequency range Δf, the ellipticity should be < -0.5 so that the left-handed polarization of the observed wave can be ensured.
- The polarization degree of all subintervals is required to be larger than 0.7 within Δf so that a large coherency of the observed wave and a high signal-to-noise ratio can be maintained.
- To ensure that the ion cyclotron mode dominates the observed wave, the maximum of the fluctuating perpendicular power density of the mean magnetic field should remain within the limits of Δf.

Figure 5 shows examples of ICWs identified from the analysis of magnetic field data of MESSENGER, which are generated by exospheric H^+ and H_2^+, adopted from Weichbold (2023), and He^+ ions at Mercury. The left panel shows the corresponding magnetic field observations in mean-field aligned coordinates. The two perpendicular magnetic field components $B_{\perp,1}$ and $B_{\perp,2}$ are coherent, and their fluctuations dominate over the variations of the parallel magnetic field component $B_{\parallel}$. This can also be seen on the right panels of Figure 4, where the perpendicular component of the power spectral density $P_{\perp}$ prevails over the parallel component $P_{\parallel}$. This indicates that the observed waves are transverse rather than compressional around the corresponding $f_{c,i}$, which is marked by the solid black lines. The area between the two dashed lines corresponds to Δf, which is used for the evaluation of the power densities, ellipticity, and polarization degree.

The propagation speeds of ICWs are less than the local Alfvén velocity v_{Alf}, which should be much lower than the injection speed v_{inj} of the pick-up ions (Delva et al., 2009). During the ICW detection, the ratio v_{Alf}/v_{inj} is also evaluated. Since the initial velocity of the exospheric neutrals before their ionization is negligible in the planetary frame, we assume that the injection velocity of the newborn exospheric ions directly corresponds to the aberrated solar wind velocity in the solar wind frame. In the following sections, we will discuss the application of the described method to Mercury, Venus, Mars, and the icy moons of the gas giants in the solar system and comets.

3 Exosphere characterization by ICW-data analysis throughout the solar system

3.1 Mercury

Mercury is considered an airless body like Earth's Moon, where the exobase level is at the planet's surface, and thus, it is directly exposed to mainly solar ions, electrons, and photons from the infrared to X-rays (Lammer et al., 2022; Wurz et al., 2022) and additionally to meteoroid fluxes (Wurz et al., 2022). The exposure of Mercury's surface to these exogenic sources modifies the surface by altering the chemical makeup and optical properties. Moreover, due to the interaction with these sources, a neutral silicate exosphere with an ionized component is produced.

3.1.1 H atoms in Mercury's extended exosphere

Until now, only two spacecraft have investigated the environment near Mercury: Mariner 10, which conducted three flybys during 1974–1975, and MESSENGER, four decades later. As briefly discussed in Section 1, early spectroscopic observations by Mariner 10 that were confirmed by MESSENGER showed that Mercury has an extended exosphere that is populated by neutral atomic hydrogen. Schmid et al. (2022) derived for the first time an altitude–density profile of the planet's extended H exosphere from *in situ* magnetic field measurements by MESSENGER. The observed H^+ ions produce the previously mentioned ICWs, which can then be identified in the magnetic field data. Schmid et al. (2022) analyzed these data and derived the local H number density that is necessary to excite the related ICWs. The results reveal an extended atomic H exosphere between ≈2,400 and 15,000 km above the surface (Schmid et al., 2022; Weichbold, 2023).

The blue dots in Figure 6A show the altitude dependence of the ICW-based and derived H atom number density from MESSENGER magnetic field data that were analyzed and adopted from Weichbold (2023). The radial distance in Mercury's radii (R_{pl} = 2,440 km) is given from the planetary center and the surface. One can see that the obtained medians decrease from ≈100 *to* 10 particles cm^{-3} between a distance of ≈2–7.5R_{pl}. Schmid et al. (2022) used a simpler approach for the calculation of the H atom profile that neglected a factor 2π and assumed an energy transfer efficiency ϕ of 100%, instead of ≈30%. Therefore, these simplifications applied by Schmid et al. (2022) resulted in H atom densities that are larger than expected in high altitudes but lie within the upper limits of the Lyman-α radiances measured by the Mariner 10 and MESSENGER spacecraft. Thus, the H atom densities shown in Figure 6A are based on Equation 2 and use an energy transfer efficiency of 30% (Cowee et al., 2007). Because of this, the ICW-based and analyzed exospheric H atom density (blue dots) is ≈ a factor of 2 lower and, as shown in Figure 6B, fits much better with the obtained Lyman-α observations of MESSENGER and Mariner 10 during their flybys (Ishak, 2019; Vervack et al., 2016).

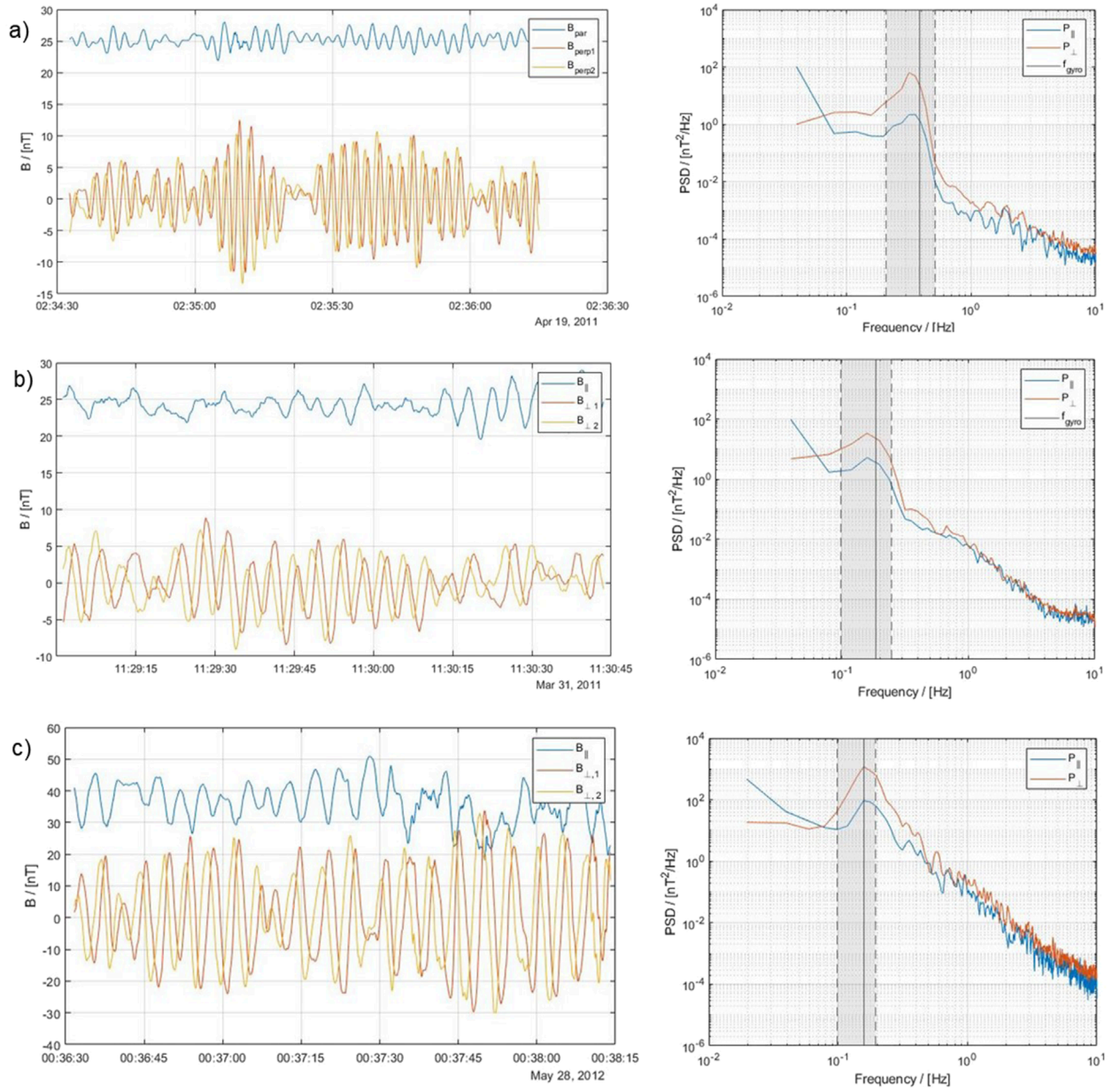

FIGURE 5
Examples of identified ICWs from MESSENGER magnetic field data and power spectra for H^+, H_2^+, and He^+ pick-up ions in Mercury's extended exosphere. Panel **(A)**: Magnetic field observation in mean-field-aligned (MFA) coordinates generated by H^+ pick-up ions, where the left figure shows the corresponding power spectrum of the H^+ ions. Panels **(B, C)** show similar data and parameters for molecular H_2^+, adopted from Weichbold (2023) and He^+ ions.

3.1.2 Exospheric H_2 molecules

Recently, Weichbold (2023) obtained the first number density profile of H_2 molecules within Mercury's exosphere from the analysis of exospheric H_2^+ pick-up ions and their related ICWs. Previous studies of H_2 based on the upper limits derived from the detection threshold of the Mariner 10 occultation data (Hunten et al., 1988; Killen and Ip, 1999; Kumar, 1976; Wurz et al., 2019) yielded upper limits for surface densities of H_2, which are $< 1.4–2.0 \times 10^7$ cm^{-3}. Schmid et al. (2022) explained the atomic hydrogen in the extended exosphere as the result of dissociation processes of H_2 molecules, which constrained the previously unknown H_2 density at the surface of Mercury to $\approx 8 \times 10^4$ cm^{-3}, which is more than two orders of magnitude lower than the values above. The first ICW-based *in situ* results yield an exospheric H_2 day-side surface density of $\approx 1.8 \times 10^3$ cm^{-3} (Weichbold, 2023).

One explanation for this result might be that the dissociation and ionization rates of H_2 are similar (Huebner and Mukherjee, 2015), such that H_2 molecules are ionized and/or dissociated in equal parts. Because of this, the H population has an additional source from the H_2 molecules, as shown in kinetic Monte Carlo simulations reported by Schmid et al. (2022). Moreover, Weichbold (2023) also investigated the possible contribution of hydrogen

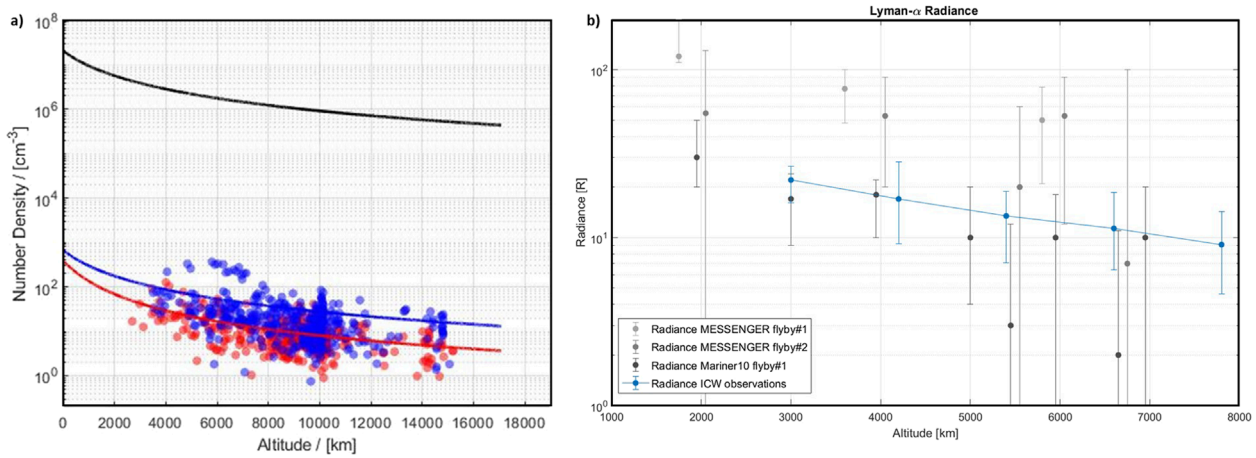

FIGURE 6
Panel **(A)**: Altitude density profiles of exospheric H atoms (blue dots) and H_2 molecules (red dots) around Mercury. The blue and red dots depict the derived H and H_2 number densities related to the analyzed ICW events, respectively. The blue and red lines correspond to the best fits obtained by an exospheric model with surface densities of 3.2×10^2 cm^{-3} for H atoms that correspond to a thermal component, dissociation products of H_2 molecules, and possibly a tiny fraction of evaporated H atoms from micrometeorites compared to a surface density of 1.8×10^3 cm^{-3} for H_2 molecules that originate mainly from thermal release at the surface (Schmid et al., 2022; Weichbold, 2023; Weichbold et al., 2025). The black line corresponds to the upper limit of Mercury's terminator number density for H_2 of 1.4×10^7 cm^{-3}, which was derived from the Mariner 10 occultation instrument threshold (Broadfoot et al., 1976). Panel **(B)**: Airglow of Lyman-α radiation from exospheric H atoms in Mercury's exosphere. The gray and black dots correspond to the Lyman-α observations of MESSENGER and Mariner 10 flybys (Ishak, 2019; Vervack et al., 2016). The blue line shows the revised Lyman-α radiances (see main text) obtained from the median (blue dot), minimal, and maximal quartile (blue error bar) of the H atom densities shown in panel **(A)**. Adopted from Weichbold (2023).

by micrometeorites. They concluded that hydrogen in Mercury's exosphere is composed of a sum of solar wind-implanted protons, related thermally released H atoms, H_2 molecules from the surface, more energetic atomic H populations arising from the dissociation of exospheric H_2 molecules, and the continuous delivery of H atoms in small proportions of carbonaceous chondrites (Wasson and Kallemeyn, 1988).

As pointed out below, ICWs generated by energetic neutral H atoms are also observed in Earth's magnetosphere environment over the polar cusp (Wei et al., 2011). Since the pick-up process inside a magnetosphere is more complex compared to a planet without an intrinsic magnetic field like Venus or Mars—due to the magnetic field variations with altitude and latitude—the observed ICWs exhibit more variable properties. Since Mercury also has an intrinsic magnetic field like Earth, one can expect that similar processes will occur in the planet's exosphere. In analogy to Earth, one can expect that a population of energetic neutral H atoms can be produced via interlinked charge exchange and ion pick-up processes over Mercury's cusp, from where they may spread into the exosphere from their source region. Exospheric H atoms will be ionized and accelerated as a picked up H^+ ion, moving from their initial point of origin to another location, where the ion can again be neutralized via charge exchange. This newly generated H atom will then be more energetic compared to its initial thermal energy and will contribute to the wide range of possible kinetic temperatures of H atoms, as shown by the blue dots in Figure 6A. A detailed study of the various expected and discussed source processes for thermal and non-thermal H atoms in Mercury's exosphere will be investigated in detail by the Mercury Planetary Orbiter (MPO) and the Mercury Magnetospheric Orbiter (MIO) during the BepiColombo mission (Benkhoff et al., 2021).

The red dots in Figure 6A show the density profile of neutral H_2 molecules in Mercury's exosphere that is derived from the analysis of related exospheric H_2^+ pick-up ions (Weichbold, 2023). One can see that the H_2 profile is orders of magnitude lower than the detection threshold of the Mariner 10 occultation data (Hunten et al., 1988). It should be noted that the remaining uncertainties or inconsistencies will be solved and measurements will be refined by future measurements of BepiColombo's MPO spacecraft using its abovementioned SERENA instrument package (Orsini et al., 2022). The known exospheric H and H_2 population will allow us to study and constrain the solar wind implantation into Mercury's regolith that leads to H, H_2, OH, and H_2O production and exospheric release and H_2O photochemistry in the ecosphere. It will allow us to investigate and separate the H_2O sources (i.e., meteoritic from solar wind implanted) and sinks on the solar system's innermost planet.

3.1.3 Mercury's extended He exosphere

He in Mercury's exosphere was first detected through remote spectroscopic observations of the Ultraviolet 14 Visible Spectrometer (UVVS) instruments in Mercury's exosphere during the Mariner 10 flybys between 1974 and 1975. Broadfoot et al. (1974), Hartle et al. (1975), Weichbold (2023), and Weichbold et al. (2025) analyzed the available MESSENGER magnetic field and plasma data from 2011–2015 and inferred *in situ* the He content in the extended exosphere between ≈0.8 and $5.74R_{pl}$. The results of these authors suggest that the majority of He in the exosphere is thermally dissolved from the surface, which includes thermal recycling of solar wind-implanted He particles. The thermal component of He has a surface density of ≈1,100 cm^{-3}. It should

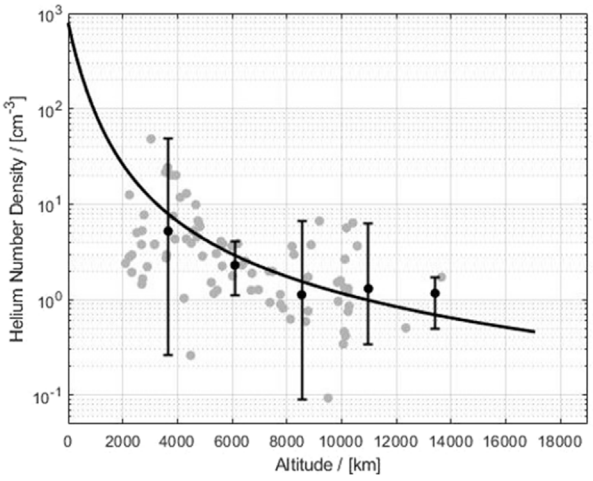

FIGURE 7
Altitude density profile of exospheric He atoms (gray dots) around Mercury. The gray dots depict the derived He number density related to analyzed ICW events that correspond toHe$^+$ pick-up ions. The black error bar indicates the minimum and maximum number densities within each 0.5 Mercury radii bin. The boxes indicate the lower and upper quartiles, and the horizontal orange lines indicate the median number density of each bin. The red line shows the best fit to the inferred densities with a Monte Carlo exosphere model. Adopted from Weichbold (2023).

also be noted that the thermal component agrees well with the observations carried out by the PHEBUS instrument onboard BepiColombo during the first Mercury swingby on October 01–02 2021 (Quémerais et al., 2023). Additionally, the data analyzed from the ICW observations also show an energetic He population with a surface density of ≈150 cm^{-3}. According to Weichbold (2025), these energetic He density enhancements beyond a planetary radius compared to the thermal profile might be caused by sporadic meteorite impact events. Figure 7 shows the reproduced and adopted He number density profiles of the thermal and energetic components, as analyzed by Weichbold (2023), and Weichbold et al. (2025), which are inferred from exospheric pick-up He$^+$ ions and the related ICWs.

3.1.4 Search and detection of meteoritic Li in the Mercury's exosphere

According to Killen et al. (2007), one can also expect that unknown components such as Li populate Mercury's exosphere. The abundance of Li in the solar system is $\approx 1 \times 10^{-3}$ (Anders and Grevesse, 1989); therefore, a low abundance in Mercury's exosphere should be expected. So far, high-resolution spectra of Mercury using the 1.5-m telescope at the Catalina Observatory near Tucson, Arizona, connected to the LPL échelle spectrograph and cooled CCD camera systems discovered no emission features at the wavelength of the Li resonance doublet at 670.8 nm. From this non-detection, Sprague et al. (1996) reported the upper limit of the Li abundance to be within an rms noise level of ≈ 0.1% in Mercury's exosphere of $< 8.4^7$ cm^{-2}.

Nearly three decades later, Schmid et al. (2025) reported for the first time the *in situ* discovery of Li in Mercury's exosphere, which is released from the surface by sporadic impact events of m-size meteoroids. The exospheric Li was discovered through the detection of Li-based ICWs, derived similarly to the aforementioned H, H_2, and He, from *in situ* magnetic field observations by the MESSENGER spacecraft. From the observation, Schmid et al. (2025) reproduced the exospheric neutral Li density at the location of the ICW generation during the meteor events. Figure 8 shows the reproduced and adopted Li density in Mercury's exosphere, as described by Schmid et al. (2025), during the 12 meteorite impact events. The range of the obtained Li surface column density lies between $\approx 5.8 \times 10^6$ cm^{-2} and 1.8×10^7 cm^{-2}, which is lower than the upper Li limit given by Sprague et al. (1996) but within the expected value at Mercury. This value is derived from meteorite ablation in Earth's mesopause, scaled to Mercury, assuming that the meteoritic Li/Na ratio of $\approx 3.3 \times 10^{-4}$ is more or less similar at the inner planet. The ratio of the detected Li during the meteoritic events to the total observed Na abundance in Mercury's exosphere is between $\approx 2.16 \times 10^{-5} - 1.76 \times 10^{-4}$, which is lower than the ratio of ordinary chondrites (Schmid et al., 2025). This difference indicates that there was much more Na in the exosphere than that was delivered by the impactors during the observed events. Moreover, from this discovery, one can suggest that micrometeorites and larger meteorites may have contaminated Mercury's upper surface layers by additions of volatile-rich material for billions of years.

3.2 Venus

In addition to available Lyman-α airglow observations shown in Figure 1B that indicate an extended hydrogen exosphere on Venus, Delva et al. (2008a) and Delva et al. (2008b) analyzed observed ICWs in the solar wind near the planetary environment. The analysis of the ICW-related data indicate that the waves are produced from H$^+$ pick-up ions that originate from exospheric H atoms over a large volume of space upstream of the planet (Delva et al., 2008a; Delva et al., 2009; Delva et al., 2015). Long-term observations over two entire Venus-years of upstream H$^+$ ICWs were analyzed, and a permanent ionization and pick-up of exospheric H atoms by the solar wind upstream of the planetary bow shock up to high altitudes were discovered (Delva et al., 2009).

However, we note that by revisiting the H$^+$ density calculations and the exosphere density estimates detailed by Delva et al. (2009), certain inconsistencies in the published data have been identified. By reproducing their published H$^+$ density and using the wave energy data from the left panel of Figure 2 of the study by Delva et al. (2009), we obtain an ion density that is approximately three orders of magnitude lower, as shown in Figure 9, than that proposed by Delva et al. (2009).The cause for this discrepancy is a unit error. For instance, the calculated H$^+$ density at two Venus radii is $\approx 4 \times 10^{-3}$ cm^{-3} and not ≈4 cm^{-3}, as given by Delva et al. (2009), which yields the roughly estimated density of atomic H of ≈20 cm^{-3}. The obtained corrected density aligns with the SPICAV data and modeled suprathermal neutral H densities, as noted by Chaufray et al. (2012), while the erroneous results shown in the right panel of Figure 2 of the study by Delva et al. (2009) result in unrealistic dense exospheric H densities. We also note that Delva et al. (2009) and Schmid et al. (2022) similarly assumed an energy transfer efficiency ϕ of 1, which also yields an overestimation of the analyzed particle density, as discussed above.

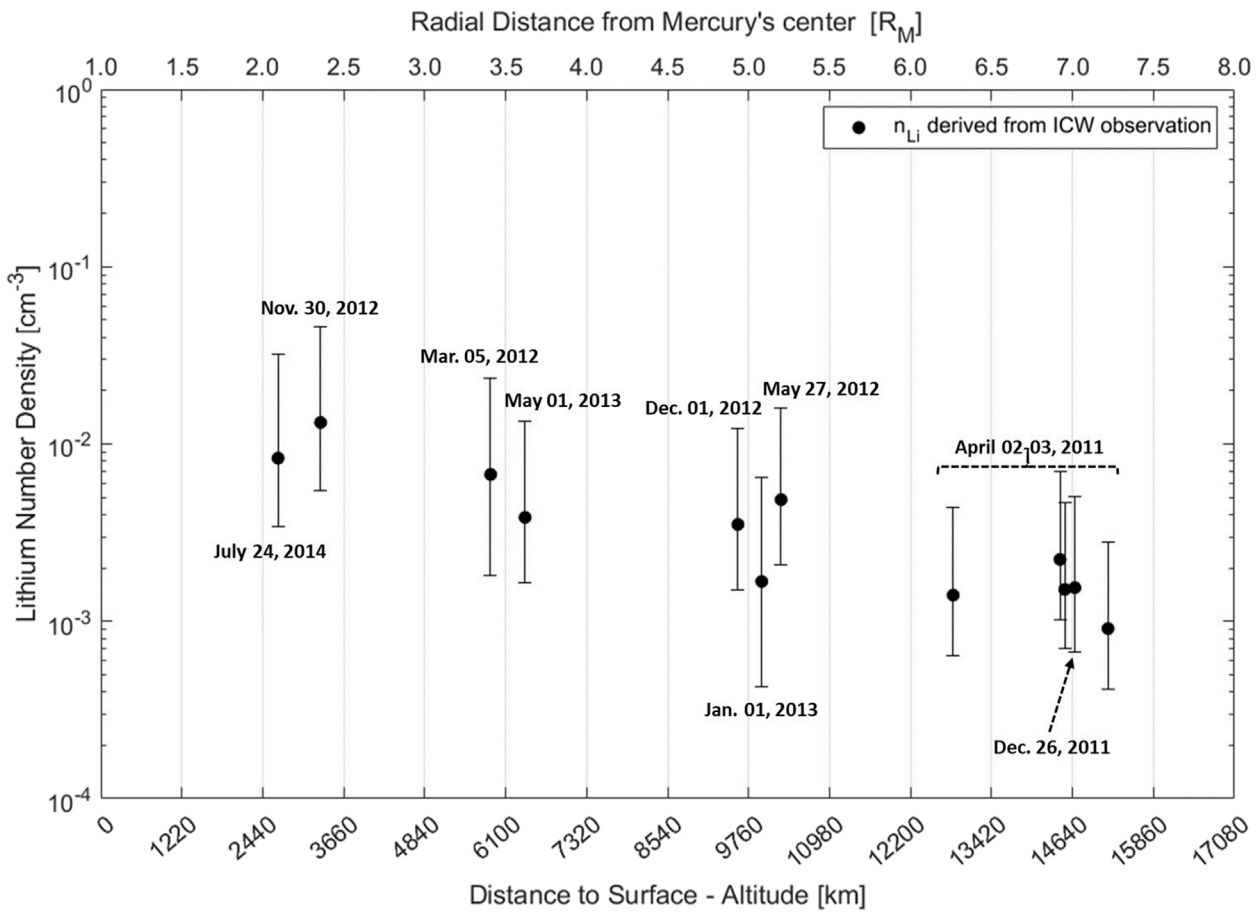

FIGURE 8
Average Li densities as a function of height (black dots, including error bars) related to the detected meteoritic impact events in Mercury's exosphere between April 2011 and July 2014. Adopted from Schmid et al. (2025).

The previously mentioned unit error and the simplified density estimations in their analysis also explain why the authors mistakenly believed that their inferred neutral gas density was much higher than expected. After the discovery and clarification of this inconsistency, we plan to soon reanalyze the plasma and magnetic field data and related ICWs in detail. This reanalysis will also include the more accurate approach and methods as described in previous sections and by Schmid et al. (2025) and Weichbold (2025). Moreover, it will also contain the search for ICWs that are generated by exospheric D^+ pick-up ions, which will help us much better understand the origin and fate of Venus' water (H_2O and HDO) inventory.

The deuterium to hydrogen (D/H) ratio on Venus shows an approximately 100-fold enrichment compared to that on Earth (Donahue et al., 1982), which is a fundamental constraint on models for its evolution of the water inventory and atmosphere (Lammer et al., 2020; Gillmann et al., 2022). From VEX, it is known that Venus has thick clouds and aerosol particles of H_2 SO_4 below the mesosphere and a light haze where CO, SO_2, HCl, HF, H_2O, and HDO are the main relevant trace species (Bertaux et al., 2007; Liang and Yung, 2009). In the Venus mesosphere, the HDO/H_2O ratio is enhanced by ≈2.5, while a depletion of H_2O is observed in the lower thermosphere at ≈80–90 km (Bertaux et al., 2007). The solar UV radiation dissociates hydrogen-bearing molecules such as H_2O and HDO at altitudes of ≈80–120 km; because of this, their abundance in the mesosphere is relevant to the total escape rate of H and D and the related evolution of the Venus water inventory, which can have its origin in carbonaceous chondrites, comets, a primordial atmosphere, or a mixture of them (Donahue, 1999)—all of them with different initial D/H ratios (Lammer et al., 2020). Crucially, if Venus had liquid water on its surface that evaporated during the latest resurfacing event ≈200–1,000 Myr ago (Kreslavsky et al., 2015), its present D/H ratio must have undergone fractionation (Donahue, 1999); otherwise, the water vapor in its present atmosphere likely originated from earlier ages in Venus' history.

For the explanation of the extended H exosphere at Venus shown in Figures 1B, 9, photochemical and charge exchange processes are responsible for the production of suprathermal H atoms (Rodriguez et al., 1984; Hodges, 1999; Lammer et al., 2006; Shematovich et al., 2014; Chaffin et al., 2024). Because suprathermal D isotopes will also undergo the same reactions and processes, one can expect that D isotopes should also populate Venus' exosphere. Contrary to Mars' exosphere, Venus exosphere does not contain H_2 molecules (Taylor et al., 1985; Hodges, 1999). D isotopes could be

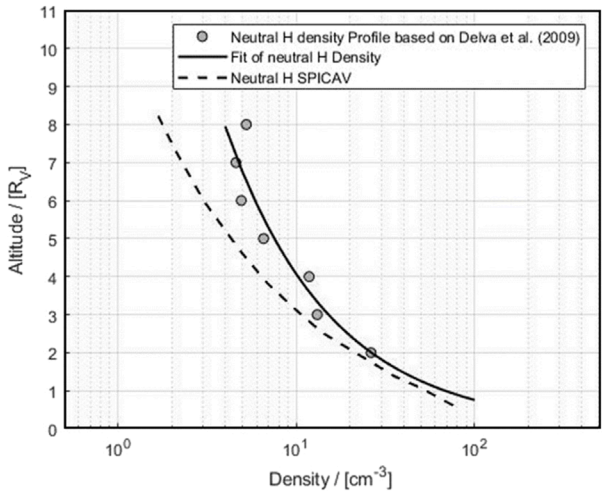

FIGURE 9
Venus' exospheric H profile (black line) inferred from H^+ pick-up generated ICWs after the correction of a unit error, as described by Delva et al. (2009), compared to the average Lyman-αbased neutral density H atom profile (dashed line) (Chaufray et al., 2012) derived from SPICAV onboard Venus Express (see also Figure 1B). The atomic H profiles agree well, but beyond 6 Venus radii, the density obtained from the ICW analysis diverges. The reasons for this deviation are because Delva et al. (2009) made only a rough density estimate and assumed energy transfer efficiency of 100%, with constant values for the solar wind speed, density, magnetic field strength, and ionization rates.

identified by future search and analysis of D^+ pick-up ion-related ICWs. Through the determination of accurate ion and neutral density profiles of H and D in Venus' exosphere from low to high solar activity by a reanalysis of H^+ and the search of D^+ ICW data, as observed by VEX magnetic field and plasma measurements, we plan to accurately determine the neutral hydrogen density in Venus' extended exosphere from the solar minimum to maximum conditions soon.

By reproducing accurate extended exospheric H and D distributions, it will, for the first time, be possible to obtain accurate loss rates of suprathermal H atoms and D atoms over the entire solar activity cycle. Together with the known ion loss rates, the total escape rates of H and D particles as a function of solar activity can finally be determined. This will also provide the ratio of H loss *versus* D loss, a crucial factor for evaluating the evolution of the D/H ratio and its connection to Venusian water inventory. The activity variation between the solar minimum and maximum can then be used as a proxy for covering the period of the Sun's average EUV flux evolution from present the day to the time Venus experienced a resurfacing event ≈200–800 million years ago and even earlier (Gillmann et al., 2022).

From this brief overview of the extended hydrogen exosphere at Venus, it is apparent that important work remains to be done to better understand and quantify the efficiency of the various processes related to the production of suprathermal hydrogen and D isotopes. This understanding is essential for reliably reconstructing and constraining the extended hydrogen and deuterium population in Venus' exosphere.

3.3 ICWs at Earth's polar cusps

Contrary to Venus, Earth possesses an intrinsic magnetic field like Mercury that builds a magnetospheric obstacle or standoff distance from the planet's surface at the subsolar point of ≈6–15 Earth radii or ≈38, 220–95,550 km, which shields the exosphere over the planet's dayside from solar wind interaction with the planet's upper atmosphere. The altitude difference Δz between Earth's exobase level at ≈500 km and the magnetospheric standoff distance at the subsolar point is ≈37, 720–95,050 km, while on Venus, Δz between the exobase level at ≈200 km and the ionopause standoff distance with its induced magnetic field is only ≈20–155 km. Thus, on Venus, the solar wind can interact near the exobase level so that ICWs can be generated in the exosphere, as discussed in Section 3.2, while on Earth, even the extended exosphere is protected from the solar wind plasma flow by magnetopause shielding. Therefore, on Earth, the solar wind can only interact over the polar cusps that are not protected by the magnetopause with the exospheric neutral particles. Russell et al. (1971), Scarf et al. (1971), and Erlandson et al. (1988) found ICWs over Earth's polar cusps at ≈4–8 Earth radii long before they were detected at other planetary bodies.

On Earth, ICWs are observed over the cusp regions in the frequency ranges of ≈4–7 Hz and ≈18–27 Hz at the locations of the OGO 5 and Viking satellites, respectively (Erlandson et al., 1988; Wei et al., 2011), between ≈2–4 Earth radii. The observed ICW frequencies correspond to the local gyrofrequencies of H^+ and alpha particles or He^{++} ions. The production of exospheric neutral particles via charge exchange between accelerated pick-up ions and neutrals is the main reason for producing an extended exosphere above Earth's polar cusps. Figure 10 shows an example of a time series and power spectra of ICWs that were observed in Earth's polar cusp by the Polar spacecraft, which were produced by H^+ pick-up ions of neutral H atoms that underwent charge exchange. Thus, on Earth, a two-step process takes place where exospheric neutral particles interact with protons over the polar areas, undergoing experience charge exchange and becoming energized. This enables them to travel away from the production region, where they are re-ionized in a subsequent process. When the energetic exospheric neutral particle population is re-ionized and picked up, they can produce a ring–beam distribution where a parallel velocity to the field can be generated (Le et al., 2001). This leads to a strong Doppler shift in the waves, which have frequencies that are much lower than the gyrofrequency. On Earth, the background magnetic field varies with altitude and latitude so that strong Doppler shifts in the waves can be produced by the pick-up ions. However, we note that the ion pick-up process in Earth's polar cusps is very complex and that the magnetic funnel around Earth's polar cusps with its curved geometry leads to more variability of ICW properties compared to planets without a strong intrinsic magnetic field, such as Venus or Mars (Le et al., 2001; Wei et al., 2011). Some new missions to study Earth's exosphere are planned to be launched or built in the near future. NASA's Carruthers Geocorona Observatory[1] will be launched in 2025; however, unfortunately, this mission has no magnetometer onboard and is therefore not suited for the detection

1 Carruthers Geocorona Observatory: https://science.nasa.gov/mission/carruthers-geocorona-observatory/

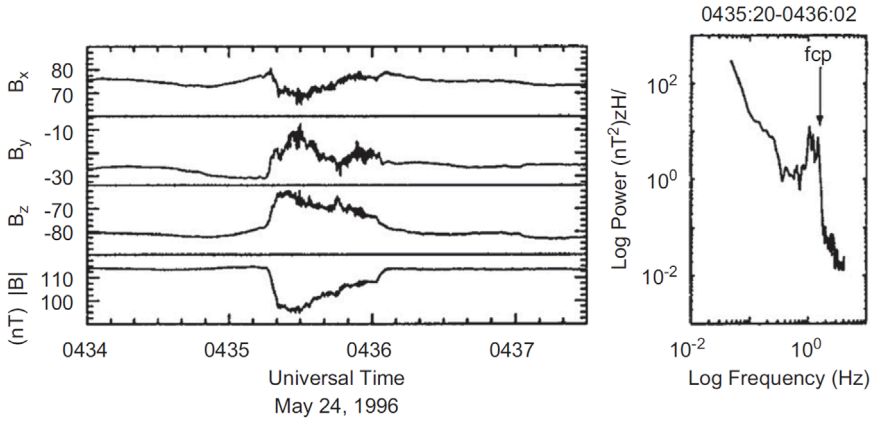

FIGURE 10
Example of a time series and power spectra of a typical H^+-induced ICW observed in Earth's polar cusp by the polar spacecraft (Le et al., 2001).

of ICWs. The same applies to China's Chang'e 6 lander on Earth's Moon, which carries the French instrument DORN (Detection of Outgassing Radon) to study the exchange of volatiles between the lunar surface and its exosphere.

3.4 Mars' extended H exosphere

On Mars, ICWs were first discovered during the Phobos mission at approximately 2–3 Mars radii with frequencies that correspond to ionized exospheric picked up hydrogen atoms (Russell et al., 1990). These findings are supported by the observations of the pick-up of H^+ ions in the extended exosphere around Mars using the ASPERA instrument (Barabash et al., 1991). Later studies that analyzed Mars Global Surveyor (MGS) magnetic field data discovered ≈500 ICW events that are generated by exospheric H^+ ions up to 14 Mars radii (Romanelli et al., 2013; Wei et al., 2014). It should also be noted that NASA's MAVEN spacecraft also detected ICWs that are generated by upstream H^+ ions in the Martian exosphere (Romanelli et al., 2016; Zhao et al., 2023; Imada et al., 2025).

Figure 11 shows an example of ICWs observed by MGS (Wei and Russell, 2006). The x-axis points from Mars to the Sun, the z-axis points upward and perpendicular to the orbital plane, and the y-axis completes a right-handed system. Similar to Mercury and Venus, the ICWs on Mars indicate that the planet has an extended hydrogen exosphere. The production of this extended hydrogen exosphere around Mars is illustrated according to Wei and Russell (2006) in Figure 11. Similar to Venus, close to Mars, exospheric H atoms are ionized and picked up due to the solar wind plasma interaction with the exosphere. This creates the detected ICWs near the planet. It is also expected that charge exchange with solar wind protons produces an energetic H atom population that is transported to greater distances where they are again re-ionized so that ICWs can be generated downstream of Mars and far to one side of the planet. Moreover, the analysis of the magnetic field and plasma data revealed an asymmetry in the direction of the interplanetary electric field, which is also found in numerical modeling (Brecht, 1990; Modolo et al., 2005). The reason for this asymmetry is related to the effects of the finite gyro radius, which is approximately 0.3 Mars radii

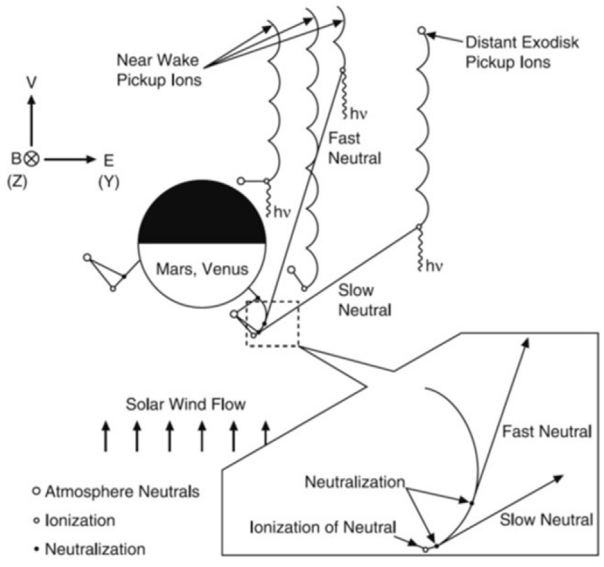

FIGURE 11
Mechanism for producing an extended H exosphere around Mars. Detailed describtions are provided in the main text [adopted from Wei and Russell (2006)].

for pick-up H^+ ions; when the particles are picked up close to the planet, the H^+ ions on the left side of Mars, as shown in Figure 11, are lost through collisions into the lower atmosphere.

Since D has also been discovered in the Martian atmosphere (Owen et al., 1988) and the D/H ratio shows that D is enriched relative to atomic H by a factor of ≈ 6, this enrichment indicates that hydrogen escaped efficiently from the planet in the past (Krasnopolsky et al., 1997; Webster et al., 2013). Similar to Venus, D escape on Mars is dominated by photochemical processes (Chaufray et al., 2024). According to the recent study by Chaufray et al. (2024), the main uncertainty in the model calculations is associated with the elastic collisional cross sections necessary to derive accurate values for the photochemical

escape rate. Therefore, we suggest that a detailed analysis of ICW data, generated by exospheric H_2^+ and D^+ pick-up ions with an atomic mass of two, may let us separate thermal H_2 molecules from higher energetic D isotopes in the upper regions of Mars' extended exosphere. The reproduction of ICW-based exospheric neutral profiles in the extended exosphere by photochemical upper atmosphere models may minimize the uncertainty in the elastic collisional cross sections mentioned above.

In the future, the 'Mars-Magnetosphere, ATmosphere, Ionosphere, and Space-weather SciencE' (M-Matisse) mission, which will study Mars using two spacecraft equipped with identical set of instruments to observe the planet simultaneously from two different locations in space, will be well-equipped to study ICWs. This mission can be used for the analysis of solar wind influences on the planet's exosphere, outer regions, the magnetic environment, and the ionosphere.

3.5 Jovian system

The giant planets in our solar system have large moons that interact with the magnetospheric plasma. These interactions can lead to the sputtering of surface particles (Watson, 1982) or volcanic activity—either magmatic, as observed in the case of Io (Smith et al., 1979; Consolmagno, 1979), or cryogenic, as observed in the cases of Europa and Enceladus (Fagents, 2003; Hansen et al., 2006). The ionization of these particles through UV radiation or electron impacts leads to pick-up by the magnetospheric magnetic field. The giant planets rotate much faster than the Keplerian velocity of the moons, and thereby, the newly generated ions are energized and create a ring (beam) distribution in velocity space, which is unstable for ICWs and mirror modes.

The pick-up ICWs at the moon of a giant planet were first detected during Galileo's Jupiter orbit insertion flyby of Io (Huddleston et al., 1997; Warnecke et al., 1997) using a magnetometer (Kivelson et al., 1992). Strong, left-handed polarized waves at the cyclotron frequency of SO_2^+ were observed during ingress and egress. Interestingly, when Galileo was within the geometrical wake of Io (i.e., the region in the magnetospheric plasma flow shade of Io), these waves disappeared and mirror modes were observed instead (Huddleston et al., 1999).

The Galileo magnetometer data were also investigated for other Galilean satellites. Because of the stronger magnetic field strengths in the Jovian magnetosphere, it is possible to measure the waves generated by heavier ions. At Europa, it was found that many different ions sputtered from the surface, such as Na, Cl, K, and SO_2, and O_2 from the tenuous Europan atmosphere (Volwerk et al., 2001). Through the analysis of the ellipticity of the waves, it was found that both left- and right-hand polarized waves were present for chlorine. This was interpreted as the pick-up of both Cl^+ and Cl^-.

A study of the three icy Galilean moons found that the pick-up and consequent generation of ICWs varies with the moon's location and the spacecraft flyby (Volwerk et al., 2010). On the upstream side of Europa, pick-up of H_2 and O^+ was detected, which possibly facilitates the slowing down of the plasma through the so-called pick-up currents given in Equation 5:

$$j_{pu} = e(\dot{n})_i \rho_L = m_i \dot{n}_i u/B, \tag{5}$$

where $\dot{n}_i$ is the pick-up rate, ρ_L is the Larmor radius, m_i is the ion mass, u is the pick-up velocity, and B is the magnetic field strength (Kivelson et al., 2009). This current will assert a force on the magnetic field through $\mathbf{J} \times \mathbf{B}$, slowing down the plasma flow. Figure 12 shows magnetic field observations at Io by the Galileo magnetometer during the flyby on 7 December 1995. In the lower panel of Figure 12, transverse ICWs in the plasma torus region are also shown.

At Ganymede, the pick-up ICW signatures are significantly less because of the internal magnetic field of this moon (Kivelson et al., 1996a;; Kivelson et al., 1996b), which creates a mini-magnetosphere with various wave modes (Volwerk et al., 1999). However, during one flyby, before Galileo entered the region of closed field lines, a broad signature around the H_2O and O cyclotron frequencies was observed.

Callisto poses a problem for the analysis of sputter ion pick-up because of the low magnetic field strength of ≈40 nT. There is a proton pick-up signature around this moon, and it is also expected that Callisto has a hydrogen component in its atmosphere (Liang et al., 2005).

In the future, the Jupiter Icy Moons Explorer (JUICE) spacecraft, expected to arrive in the Jupiter system in 2031, is anticipated to investigate ICWs and exospheric species of the icy satellites through correlated efforts involving the Jovian-magnetometer (J-MAG), the Radio and Plasma Wave Investigation (RPWI), and the Particle Environment Package (PEP) instruments, along with their teams.

3.6 Kronian system

Saturn's system consists of a multitude of moons and rings, including well-known objects like Titan, Enceladus, the E-ring, and, more recently, Mimas, which is expected to have a recently formed ocean underneath its icy crust (Lainey et al., 2024).

The first evidence for ICWs in the Kronian system came from Pioneer 11 observations in the E-ring in the neighborhood of Dione's L-shell (Smith and Tsurutani, 1983), and although the generation mechanism is assumed to be the ion cyclotron resonance, these are not from local pick-up of freshly ionized particles but likely generated by a temperature anisotropy in the O^+ distribution.

Cassini, with its magnetometer (Dougherty et al., 2004), flew over the E-ring and measured clear ICWs around frequencies of water-group ions (H_3 O^+, H_2 O^+, OH^+, and O^+). These waves are generated through the pick-up of ionized neutrals in the E-ring's exosphere (Leisner et al., 2006). These waves are present independent of the tilt direction of Saturn's rotational axis concerning the Sun, which leads to the conclusion that charge exchange and electron-impact ionization are more important than photo-ionization.

Enceladus was found to have water plumes in its southern hemisphere (Porco et al., 2006), which also had a clear signature in the magnetometer measurements (Dougherty et al., 2006). During two Enceladus flybys, there were clear cyclotron wave signatures in the magnetometer data, mainly downstream of the moon. The period of the waves is consistent with the pick-up of H_2O-group ions (Tokar et al., 2008). Pick-up ion signatures were measured near Titan using a Cassini Plasma Spectrometer/ion mass spectrometer (CAPS/IMS) (McComas et al., 2010). The presence of various heavy

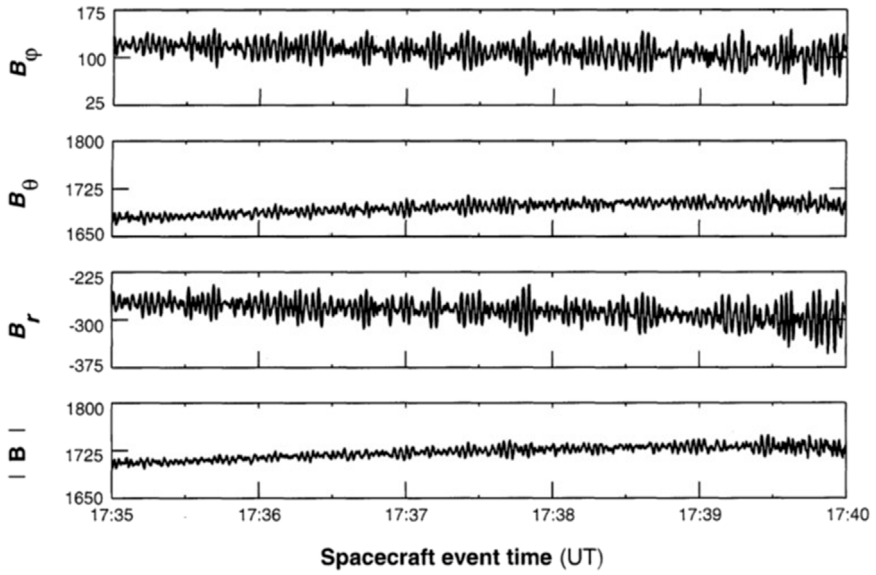

FIGURE 12
Observed ICWs in the vicinity of Io. Expanded data from 17:35 to 17:40 UT (Kivelson et al., 1996c).

pick-up ions with ≈16 ≤ m/q ≤ ≈ 28 corresponded to CH_3^+ and N_2^+ but also lighter species with $m/q = 2$ H_2^+ (Regoli et al., 2016).

However, the detection of ICWs remained elusive in the almost 100 flybys of Titan by Cassini. Only two events have been found during the T63 and T98 flybys (Russell et al., 2016): in the former, H_2^+ and H^+ ICWs were present, while in the latter, only H^+ ICWs were observed, with small wave amplitudes (≤0.1 nT). Presumably, the lack of ICW observations near Titan is caused by the variability in the magnetic field in the neighborhood of Titan, which buries the ICW signatures in the noise (Cowee et al., 2010). This magnetic field variability and the related noise near Titan prevent the reproduction of neutral density profiles in Saturn's large moon's extended exosphere.

3.7 Comets

Comets start their outgassing when their orbits cross Jupiter's orbit when the solar irradiance is strong enough to start the sublimation of volatiles in the nucleus. This neutral gas cloud that is created reacts with the solar UV radiation and gets ionized, and it will also interact with the solar wind, creating a bow shock and a coma, various boundaries, and the diamagnetic cavity (Goetz et al., 2022; Goetz et al., 2023).

The freshly ionized particles in the coma will be picked up by the solar wind and can generate ICWs. There have been a few missions to comets: Giotto encountered comet 27P/Grigg–Skjellerup, and ICWs were measured near the H_2 O^+ frequency (Neubauer et al., 1993; Glassmeier and Neubauer, 1993; Glassmeier et al., 1993; Coates et al., 1993). At the main target of Giotto, comet 1P/Halley, no cyclotron waves were observed; however, hydromagnetic waves near the O^+ or H_2 O^+ cyclotron frequency were observed by Sakigake, which was further away from the nucleus than Giotto (Yumoto and Nakagawa, 1986). Using data from the VEGA spacecraft at comet 1P/Halley and from ICE at comet 21P/Giacomini–Zinner, some indication was found for power at the H^+ and H_2 O^+ cyclotron frequency (Le et al., 1989).

During the Rosetta mission around comet 67P/Churyumov–Gerasimenko, no evidence of ICWs was obtained from the magnetometer data, which could be caused by the relatively weak outgassing rates at approach and the too-short transport time of the picked up ions for the waves to grow to a detectable level. Because the target body for the Comet Interceptor mission at the end of this decade is not yet known (Jones et al., 2024), it is not clear if ICWs and related research can be carried out for the characterization of the Comet Interceptor's target. However, one can speculate that the novelty of three-point magnetic measurements when the Comet Interceptor mission is fully deployed in and around the target comet, albeit a nominal mission duration of at most a few hours, will allow us to derive a spatial and temporal distribution of cometary exospheric species from hydrogen to heavier neutral molecular species.

4 Conclusion

We have shown that a detailed analysis of observed ion cyclotron waves generated by exospheric pick-up ions can be used to derive the neutral densities of exospheric particles in extended exosphere layers. The method is mainly applicable to light elements (H, H_2, D, He, etc.) and is limited by the gyroradius of the investigated particles and magnetic field fluctuations near the planetary body.

The gyroradii of the exospheric pick-up ions should be less than the radius of the planetary bodies so that one can reproduce enough data points related to the study of exospheric particles. On Mercury, ICW-related analysis of data obtained by the MESSENGER can retrieve H, H_2, and He density profiles in the planet's extended exosphere, and the detection of exospheric Li during meteoritic impacts. On Venus and Mars, ICWs related to pick-up H^+ ions were discovered, and on Venus, the extended neutral H atom density in the planet's extended exosphere is roughly in agreement with the Lyman-α based neutral H atom density profile derived from VEX. In the future, ICWs that belong to deuterium should be searched, and the H, H_2, and D density profiles in the exospheres of both planets may be derived. An accurate reproduction of the planet's D and H density profiles will constrain the losses of both species and allow deducing the D/H ratio, hence estimating the water loss over time on these planets in a realistic way. Finally, future observations of ICWs by BepiColombo at Mercury, the satellites of the gas giants by the JUICE spacecraft, and Comet Interceptor in combination with spectroscopic methods and particle detectors will certainly help characterize the dynamic of exospheres of terrestrial bodies throughout the solar system.

Author contributions

HL: conceptualization, investigation, writing–original draft, and writing–review and editing. DS: data curation, investigation, methodology, software, visualization, and writing–review and editing. MV: investigation, methodology, and writing–review and editing. FW: methodology, visualization, and writing–review and editing. CW: investigation and writing–review and editing. AV: investigation and writing–review and editing. MD: methodology and writing–review and editing.

Funding

The author(s) declare that financial support was received for the research, authorship, and/or publication of this article. HL and FW thank the Austrian Science Fund (FWF) for the support of the VeReDo research project, grant I6857N. CW was funded by the Austrian Science Fund (FWF) project 10.55776/P35954.

Conflict of interest

The authors declare that the research was conducted in the absence of any commercial or financial relationships that could be construed as a potential conflict of interest.

The author(s) declared that they were an editorial board member of Frontiers, at the time of submission. This had no impact on the peer review process and the final decision.

Publisher's note

References

Anders, E., and Grevesse, N. (1989). Abundances of the elements: meteoritic and solar. *Geochim. Cosmochim. Acta* 53, 197–214. doi:10.1016/0016-7037(89)90286-X

Anderson, J., and Donald, E. (1976). The mariner 5 ultraviolet photometer experiment: analysis of hydrogen lyman-alpha data. *J. Geophys. Res.* 81, 1213–1216. doi:10.1029/JA081i007p01213

Anderson, J., Donald, E., and Hord, C. W. (1971). Mariner 6 and 7 ultraviolet spectrometer experiment: analysis of hydrogen lyman-alphaalpha data. *J. Geophys. Res.* 76, 6666. doi:10.1029/JA076i028p06666

Arthur, C. W., McPherron, R. L., and Means, J. D. (1976). A comparative study of three techniques for using the spectral matrix in wave analysis. *Radio Sci.* 11, 833–845. doi:10.1029/RS011i010p00833

Barabash, S., Dubinin, E., Pisarenko, N., Lundin, R., and Russell, C. T. (1991). Picked-up protons near Mars: Phobos observations. *Geophys. Res. Lett.* 18, 1805–1808. doi:10.1029/91GL02082

Barabash, S., Fedorov, A., Lundin, R., and Sauvaud, J.-A. (2007). Martian atmospheric erosion rates. *Science* 315, 501–503. doi:10.1126/science.1134358

Barabash, S., Lundin, R., Andersson, H., Gimholt, J., Holmström, M., Norberg, O., et al. (2004). "ASPERA-3: analyser of space plasmas and energetic ions for Mars Express," in *Mars express: the scientific payload*. Editors A. Wilson, and A. Chicarro (Noordwijk, Netherlands: ESA Special Publication), 1240, 121–139.

Barth, C. A., Fastie, W. G., Hord, C. W., Pearce, J. B., Kelly, K. K., Stewart, A. I., et al. (1969). Mariner 6: ultraviolet spectrum of Mars upper atmosphere. *Science* 165, 1004–1005. doi:10.1126/science.165.3897.1004

Bauer, S. J., and Lammer, H. (2004). *Planetary aeronomy: atmosphere environments in planetary systems*. Berlin, Heidelberg, New York: Springer.

Benkhoff, J., Murakami, G., Baumjohann, W., Besse, S., Bunce, E., Casale, M., et al. (2021). BepiColombo - mission overview and science goals. *Space Sci. Rev.* 217, 90. doi:10.1007/s11214-021-00861-4

Bertaux, J. L., Blamont, J., Marcelin, M., Kurt, V. G., Romanova, N. N., and Smirnov, A. S. (1978). Lyman-alpha observations of venera-9 and 10 I. The non-thermal hydrogen population in the exosphere of venus. *Planet. Space Sci.* 26, 817–831. doi:10.1016/0032-0633(78)90105-8

Bertaux, J. L., Lepine, V. M., Kurt, V. G., and Smirnov, A. S. (1982). Altitude profile of H in the atmosphere of Venus from Lyman α observations of Venera 11 and Venera 12 and origin of the hot exospheric component. *Icarus* 52, 221–244. doi:10.1016/0019-1035(82)90110-5

Bertaux, J.-L., Vandaele, A.-C., Korablev, O., Villard, E., Fedorova, A., Fussen, D., et al. (2007). A warm layer in Venus' cryosphere and high-altitude measurements of HF, HCl, H_2O and HDO. *Nature* 450, 646–649. doi:10.1038/nature05974

Bertucci, C., Mazelle, C., and Acuña, M. H. (2005). Interaction of the solar wind with Mars from Mars global surveyor MAG/ER observations. *J. Atmos. Solar-Terrest. Phys.* 67, 1797–1808. doi:10.1016/j.jastp.2005.04.007

Bida, T. A., Killen, R. M., and Morgan, T. H. (2000). Discovery of calcium in Mercury's atmosphere. *Nature* 404, 159–161. doi:10.1038/35004521

Brecht, S. H. (1990). Magnetic asymmetries of unmagnetized planets. *Geophys. Res. Lett.* 17, 1243–1246. doi:10.1029/GL017i009p01243

Broadfoot, A. L., Kumar, S., Belton, M. J. S., and McElroy, M. B. (1974). Mercury's atmosphere from mariner 10: preliminary results. *Science* 185, 166–169. doi:10.1126/science.185.4146.166

Broadfoot, A. L., Shemansky, D. E., and Kumar, S. (1976). Mariner 10: Mercury atmosphere. *Geophys. Res. Lett.* 3, 577–580. doi:10.1029/GL003i010p00577

Chaffin, M. S., Cangi, E. M., Gregory, B. S., Yelle, R. V., Deighan, J., Elliott, R. D., et al. (2024). Venus water loss is dominated by HCO^+ dissociative recombination. *Nature* 629, 307–310. doi:10.1038/s41586-024-07261-y

Chamberlain, J. W. (1963). Planetary coronae and atmospheric evaporation. *Planet. Space Sci.* 11, 901–960. doi:10.1016/0032-0633(63)90122-3

Chaufray, J. Y., Bertaux, J. L., Quémerais, E., Villard, E., and Leblanc, F. (2012). Hydrogen density in the dayside venusian exosphere derived from Lyman-α observations by SPICAV on Venus Express. *Icarus* 217, 767–778. doi:10.1016/j.icarus.2011.09.027

Chaufray, J. Y., Gonzalez-Galindo, F., Leblanc, F., Modolo, R., Vals, M., Montmessin, F., et al. (2024). Simulations of the hydrogen and deuterium thermal and non-thermal escape at Mars at Spring Equinox. *Icarus* 418, 116152. doi:10.1016/j.icarus.2024.116152

Chirakkil, K., Deighan, J., Chaffin, M. S., Jain, S. K., Lillis, R. J., Raghuram, S., et al. (2024). EMM EMUS observations of hot oxygen corona at Mars: radial distribution and temporal variability. *J. Geophys. Res. Space Phys.* 129, e2023JA032342. doi:10.1029/2023JA032342

Coates, A. J., Johnstone, A. D., Huddleston, D. E., Wilken, B., Jockers, K., Borg, H., et al. (1993). Pickup water group ions at comet Grigg-Skjellerup. *Geophys. Res. Lett.* 20, 483–486. doi:10.1029/93gl00174

Coates, A. J., Johnstone, A. D., Kessel, R. L., Huddleston, D. E., and Wilken, B. (1990). Plasma parameters near the Comet Halley bow shock. *J. Geophys. Res.* 95, 20701–20716. doi:10.1029/JA095iA12p20701

Consolmagno, G. J. (1979). Sulfur volcanoes on Io. *Science* 205, 397–398. doi:10.1126/science.205.4404.397

Cowee, M. M., and Gary, S. P. (2012). Electromagnetic ion cyclotron wave generation by planetary pickup ions: one-dimensional hybrid simulations at sub-Alfvénic pickup velocities. *J. Geophys. Res. Space Phys.* 117, A06215. doi:10.1029/2012JA017568

Cowee, M. M., Gary, S. P., and Wei, H. Y. (2012). Pickup ions and ion cyclotron wave amplitudes upstream of Mars: first results from the 1D hybrid simulation. *Geophys. Res. Lett.* 39, L08104. doi:10.1029/2012GL051313

Cowee, M. M., Gary, S. P., Wei, H. Y., Tokar, R. L., and Russell, C. T. (2010). An explanation for the lack of ion cyclotron wave generation by pickup ions at Titan: 1-D hybrid simulation results. *J. Geophys. Res.* 115, A10224. doi:10.1029/2010JA015769

Cowee, M. M., Russell, C. T., Strangeway, R. J., and Blanco-Cano, X. (2007). One-dimensional hybrid simulations of obliquely propagating ion cyclotron waves: application to ion pickup at Io. *J. Geophys. Res. Space Phys.* 112, A06230. doi:10.1029/2006JA012230

Cravens, T. E., Gombosi, T., and Nagy, A. F. (1980). Hot hydrogen in the exosphere of Venus. *Nature* 283, 178–180. doi:10.1038/283178a0

Deighan, J., Chaffin, M. S., Chaufray, J. Y., Stewart, A. I. F., Schneider, N. M., Jain, S. K., et al. (2015). MAVEN IUVS observation of the hot oxygen corona at Mars. *Geophys. Res. Lett.* 42, 9009–9014. doi:10.1002/2015GL065487

Delva, M., Bertucci, C., Volwerk, M., Lundin, R., Mazelle, C., and Romanelli, N. (2015). Upstream proton cyclotron waves at Venus near solar maximum. *J. Geophys. Res. Space Phys.* 120, 344–354. doi:10.1002/2014JA020318

Delva, M., Mazelle, C., and Bertucci, C. (2011). Upstream ion cyclotron waves at venus and Mars. *Space Sci. Rev.* 162, 5–24. doi:10.1007/s11214-011-9828-2

Delva, M., Volwerk, M., Mazelle, C., Chaufray, J. Y., Bertaux, J. L., Zhang, T. L., et al. (2009). Hydrogen in the extended venus exosphere. *Geophys. Res. Lett.* 36, L01203. doi:10.1029/2008GL036164

Delva, M., Zhang, T. L., Volwerk, M., Magnes, W., Russell, C. T., and Wei, H. Y. (2008a). First upstream proton cyclotron wave observations at Venus. *Geophys. Res. Lett.* 35, L03105. doi:10.1029/2007GL032594

Delva, M., Zhang, T. L., Volwerk, M., Vörös, Z., and Pope, S. A. (2008b). Proton cyclotron waves in the solar wind at Venus. *J. Geophys. Res. (Planets)* 113, E00B06. doi:10.1029/2008JE003148

Donahue, T. M. (1999). New analysis of hydrogen and deuterium escape from venus. *Icarus* 141, 226–235. doi:10.1006/icar.1999.6186

Donahue, T. M., Hoffman, J. H., Hodges, R. R., and Watson, A. J. (1982). Venus was wet: a measurement of the ratio of deuterium to hydrogen. *Science* 216, 630–633. doi:10.1126/science.216.4546.630

Dougherty, M. K., Kellock, S., Southwood, D. J., Balogh, A., Tsurutani, E. J. S. B. T., Gerlach, B., et al. (2004). The Cassini magnetic field investigation. *Space Sci. Rev.* 114, 331–383. doi:10.1007/978-1-4020-2774-1_4

Dougherty, M. K., Khurana, K. K., Neubauer, F. M., Russell, C. T., Saur, J., Leisner, J. S., et al. (2006). Identification of a dynamic atmosphere at Enceladus with the Cassini magnetometer. *Science* 311, 1406–1409. doi:10.1126/science.1120985

Erlandson, R. E., Zanetti, L. J., Potemra, T. A., Andre, M., and Matson, L. (1988). Observation of electromagnetic ion cyclotron waves and hot plasma in the polar cusp. *Geophys. Res. Lett.* 15, 421–424. doi:10.1029/GL015i005p00421

Fagents, S. A. (2003). Considerations for effusive cryovolcanism on Europa: the post-Galileo perspective. *J. Geophys. Res.* 108, 5139. doi:10.1029/2003JE002128

Fränz, M., Echer, E., Marques de Souza, A., Dubinin, E., and Zhang, T. L. (2017). Ultra low frequency waves at venus: observations by the venus express spacecraft. *Planet. Space Sci.* 146, 55–65. doi:10.1016/j.pss.2017.08.011

Galli, A., Wurz, P., Kallio, E., Ekenbäck, A., Holmström, M., Barabash, S., et al. (2008). Tailward flow of energetic neutral atoms observed at Mars. *J. Geophys. Res. (Planets)* 113, E12012. doi:10.1029/2008JE003139

Gary, S. P. (1991). Electromagnetic ion/ion instabilities and their consequences in space plasmas - a review. *Space Sci. Rev.* 56, 373–415. doi:10.1007/BF00196632

Gary, S. P., and Winske, D. (1993). Simulations of ion cyclotron anisotropy instabilities in the terrestrial magnetosheath. *J. Geophys. Res.* 98, 9171–9179. doi:10.1029/93JA00272

Gillmann, C., Way, M. J., Avice, G., Breuer, D., Golabek, G. J., Höning, D., et al. (2022). The long-term evolution of the atmosphere of venus: processes and feedback mechanisms. *Space Sci. Rev.* 218, 56. doi:10.1007/s11214-022-00924-0

Glassmeier, K. H., Motschmann, U., Mazalle, C., Neubauer, F. M., Sauer, K., Fuselier, S. A., et al. (1993). Mirror modes and fast magnetoaucoustic waves near the magnetic pileup boundary of comet P/Halley. *J. Geophys. Res.* 98, 20955–20964. doi:10.1029/93JA02582

Glassmeier, K.-H., and Neubauer, F. M. (1993). Low-frequency electromagnetic plasma waves at comet P/Grigg-Skjellerup: overview and spectral characteristics. *J. Geophys. Res.* 98, 20921–20935. doi:10.1029/93ja02583

Goetz, C., Behar, E., beth, A., Bodewits, D., Bromley, S., Burch, J., et al. (2022). The plasma environment of comet 67P/Churyumov-Gerasimenko. *Space Sci. Rev.* 218, 65. doi:10.1007/s11214-022-00931-1

Goetz, C., Gunell, H., Volwerk, M., Beth, A., Erkisson, A., Galand, M., et al. (2023). Cometary plasma science - open science questions for future space missions. *Exp. Astro.* 54, 1129–1167. doi:10.1007/s10686-021-09783-z

Grasset, O., Dougherty, M. K., Coustenis, A., Bunce, E. J., Erd, C., Titov, D., et al. (2013). JUpiter ICy moons Explorer (JUICE): an ESA mission to orbit Ganymede and to characterise the Jupiter system. *Planet. Space Sci.* 78, 1–21. doi:10.1016/j.pss.2012.12.002

Halekas, J. S. (2017). Seasonal variability of the hydrogen exosphere of Mars. *J. Geophys. Res. (Planets)* 122, 901–911. doi:10.1002/2017JE005306

Halekas, J. S., and McFadden, J. P. (2021). Using solar wind helium to probe the structure and seasonal variability of the martian hydrogen corona. *J. Geophys. Res. (Planets)* 126, e07049. doi:10.1029/2021je007049

Halekas, J. S., Taylor, E. R., Dalton, G., Johnson, G., Curtis, D. W., McFadden, J. P., et al. (2015). The solar wind ion analyzer for MAVEN. *Space Sci. Rev.* 195, 125–151. doi:10.1007/s11214-013-0029-z

Hansen, C. J., Esposito, L., Stewart, A. I. F., Colwell, J., Hendrix, A., Pryor, W., et al. (2006). Enceladus' water vapor plume. *Science* 311, 1422–1425. doi:10.1126/science.1121254

Hartle, R. E., Curtis, S. A., and Thomas, G. E. (1975). Mercury's helium exosphere. *J. Geophys. Res.* 80, 3689–3692. doi:10.1029/JA080i025p03689

Hodges, R. R. (1999). An exospheric perspective of isotopic fractionation of hydrogen on Venus. *J. Geophys. Res.* 104, 8463–8471. doi:10.1029/1999JE900006

Holsclaw, G. M., Deighan, J., Almatroushi, H., Chaffin, M., Correira, J., Evans, J. S., et al. (2021). The Emirates Mars ultraviolet spectrometer (EMUS) for the EMM mission. *Space Sci. Rev.* 217, 79. doi:10.1007/s11214-021-00854-3

Huddleston, D. E., Coates, A. J., and Johnstone, A. D. (1992a). Correction to 'Predictions of the solar wind interaction with comet Grigg-Skjellerup by eds D. E. Huddleston, and A. J. Coates, *A. D. Johnst. Geophys. Res. Lett.* 19, 1319. doi:10.1029/92GL01330

Huddleston, D. E., Coates, A. J., and Johnstone, A. D. (1992b). Predictions of the solar wind interaction with Comet Grigg-Skjellerup. *Geophys. Res. Lett.* 19, 837–840. doi:10.1029/92GL00639

Huddleston, D. E., and Johnstone, A. D. (1992). Relationship between wave energy and free energy from pickup ions in the Comet Halley Environment. *J. Geophys. Res.* 97, 12217–12230. doi:10.1029/92JA00726

Huddleston, D. E., Strangeway, R. J., Warnecke, J., Russell, C. T., and Kivelson, M. G. (1998). Ion cyclotron waves in the Io torus: wave dispersion, free energy analysis, and SO_2^+ source rate estimates. *J. Geophys. Res.* 103, 19887–19899. doi:10.1029/97JE03557

Huddleston, D. E., Strangeway, R. J., Warnecke, J., Russell, C. T., Kivelson, M. G., and Bagenal, F. (1997). Ion cyclotron waves in the Io torus during the Galileo encounter: warm plasma dispersion analysis. *Geophys. Res. Lett.* 24, 2143–2146. doi:10.1029/97GL01203

Huddleston, D. E., Strangway, R. J., Blanco-Cano, X., Russell, C. T., Kivelson, M. G., and Khurana, K. K. (1999). Mirror-mode structures at the Galileo-Io flyby: instability criterion and dispersion analysis. *J. Geophys. Res.* 104, 17479–17489. doi:10.1029/1999JA900195

Huebner, W. F., and Mukherjee, J. (2015). Photoionization and photodissociation rates in solar and blackbody radiation fields. *Planet. Space Sci.* 106, 11–45. doi:10.1016/j.pss.2014.11.022

Hunten, D. M., Morgan, T. H., and Shemansky, D. E. (1988). The Mercury atmosphere.

Imada, K., Harada, Y., Fowler, C. M., Collinson, G., Halekas, J. S., Ruhunusiri, S., et al. (2025). Magnetosonic waves in the Martian ionosphere driven by upstream proton cyclotron waves: two-point observations by MAVEN and Mars Express. *Icarus* 425, 116311. doi:10.1016/j.icarus.2024.116311

Ishak, B. (2019). Mercury: the view after MESSENGER. *Taylor Francis* 60, 341. doi:10.1080/00107514.2019.1709557

Jakosky, B. M., Brain, D., Chaffin, M., Curry, S., Deighan, J., Grebowsky, J., et al. (2018). Loss of the martian atmosphere to space: present-day loss rates determined from maven observations and integrated loss through time. *Icarus* 315, 146–157. doi:10.1016/j.icarus.2018.05.030

Jones, G. H., Snodgrass, C., Tubiana, C., Küppers, M., Kawakita, H., Lara, L. M., et al. (2024). The comet interceptor mission. *Space Sci. Rev.* 220, 9. doi:10.1007/s11214-023-01035-0

Killen, R., Cremonese, G., Lammer, H., Orsini, S., Potter, A. E., Sprague, A. L., et al. (2007). Processes that promote and deplete the exosphere of Mercury. *Space Sci. Rev.* 132, 433–509. doi:10.1007/s11214-007-9232-0

Killen, R. M., and Ip, W.-H. (1999). The surface-bounded atmospheres of Mercury and the Moon. *Rev. Geophys.* 37, 361–406. doi:10.1029/1999RG900001

Kivelson, M. G., Khurana, K. K., Means, J. D., Russell, C. T., and Snare, R. C. (1992). The galileo magnetic field investigation. *Space Sci. Rev.* 60, 357–383. doi:10.1007/bf00216862

Kivelson, M. G., Khurana, K. K., Russell, C. T., Walker, R. J., Warnecke, J., Coroniti, F. V., et al. (1996a). Discovery of Ganymede's magnetic field by the Galileo spacecraft. *Nature* 384, 537–541. doi:10.1038/384537a0

Kivelson, M. G., Khurana, K. K., and Volwerk, M. (2009). "Europa's interaction with the Jovian magnetosphere," in *Europa*. Editors R. T. Pappalardo, W. B. McKinnon, and K. K. Khurana (Tucson, USA: University of Arizona Press), 545–570.

Kivelson, M. G., Khurana, K. K., Walker, R. J., Russell, C. T., Linker, J. A., Southwood, D. J., et al. (1996b). A magnetic signature at Io: initial report from the galileo magnetometer. *Science* 273, 337–340. doi:10.1126/science.273.5273.337

Kivelson, M. G., Khurana, K. K., Walker, R. J., Warnecke, J., Russell, C. T., Linker, J. A., et al. (1996c). Io's Interaction with the plasma torus: galileo magnetometer report. *Science* 5286, 396–398. doi:10.1126/science.274.5286.396

Krasnopolsky, V. A., Bjoraker, G. L., Mumma, M. J., and Jennings, D. E. (1997). High-resolution spectroscopy of Mars at 3.7 and 8 μm: a sensitive search of H_2O_2, H_2CO, HCl, and CH_4, and detection of HDO. *J. Geophys. Res.* 102, 6525–6534. doi:10.1029/96JE03766

Kreslavsky, M. A., Ivanov, M. A., and Head, J. W. (2015). The resurfacing history of Venus: constraints from buffered crater densities. *Icarus* 250, 438–450. doi:10.1016/j.icarus.2014.12.024

Kumar, S. (1976). Mercury's atmosphere: a perspective after mariner 10. *Icarus* 28, 579–591. doi:10.1016/0019-1035(76)90131-7

Lainey, V., Rambaux, N., Tobie, G., Cooper, N., Zhang, Q., Noyelles, B., et al. (2024). A recently formed ocean inside Saturn's moon Mimas. *Nature* 626, 280–282. doi:10.1038/s41586-023-06975-9

Lammer, H. (2013). "Origin and evolution of planetary atmospheres," in *Springer briefs in astrobiology*. Springer. doi:10.1007/978-3-642-32087-3

Lammer, H., Lichtenegger, H. I. M., Biernat, H. K., Erkaev, N. V., Arshukova, I. L., Kolb, C., et al. (2006). Loss of hydrogen and oxygen from the upper atmosphere of Venus. *Planet. Space Sci.* 54, 1445–1456. doi:10.1016/j.pss.2006.04.022

Lammer, H., Scherf, M., Ito, Y., Mura, A., Vorburger, A., Guenther, E., et al. (2022). The exosphere as a boundary: origin and evolution of airless bodies in the inner solar system and beyond including planets with silicate atmospheres. *Space Sci. Rev.* 218, 15. doi:10.1007/s11214-022-00876-5

Lammer, H., Scherf, M., Kurokawa, H., Ueno, Y., Burger, C., Maindl, T., et al. (2020). Loss and fractionation of noble gas isotopes and moderately volatile elements from planetary embryos and early venus, Earth and Mars. *Space Sci. Rev.* 216, 74. doi:10.1007/s11214-020-00701-x

Le, G., Blanco-Cano, X., Russell, C. T., Zhou, X. W., Mozer, F., Trattner, K. J., et al. (2001). Electromagnetic ion cyclotron waves in the high altitude cusp: polar observations. *J. Geophys. Res.* 106, 19067–19079. doi:10.1029/2000JA900163

Le, G., Russell, C. T., Gary, S. P., Smith, E. J., Riedler, W., and Schwingenschuh, K. (1989). ULF waves at comets Halley and Giacobini-Zinner: comparison with theory. *Adv. Space Res.* 9, 373–376. doi:10.1016/0273-1177(89)90292-5

Leblanc, F., Doressoundiram, A., Schneider, N., Massetti, S., Wedlund, M., López Ariste, A., et al. (2009). Short-term variations of Mercury's Na exosphere observed with very high spectral resolution. *Geophys. Res. Lett.* 36, L07201. doi:10.1029/2009GL038089

Leisner, J. S., Russell, C. T., Dougherty, M. K., Blanco-Cano, X., Strangeway, R. J., and Bertucci, C. (2006). Ion cyclotron waves in Saturn's E ring: initial Cassini observations. *Geophys. Res. Lett.* 33, L11101. doi:10.1029/2005GL024875

Liang, M.-C., Lane, B. F., Pappalardo, R. T., Alan, M., and Yung, Y. L. (2005). Atmosphere of Callisto. *J. Geophys. Res.* 110, E02003. doi:10.1029/2004je002322

Liang, M.-C., and Yung, Y. L. (2009). Modeling the distribution of H_2O and HDO in the upper atmosphere of Venus. *J. Geophys. Res.* 114, E00B28. doi:10.1029/2008JE003095

Lichtenegger, H. I. M., Lammer, H., Kulikov, Y. N., Kazeminejad, S., Molina-Cuberos, G. H., Rodrigo, R., et al. (2006). Effects of low energetic neutral atoms on martian and venusian dayside exospheric temperature estimations. *Space Sci. Rev.* 126, 469–501. doi:10.1007/s11214-006-9082-1

Luhmann, J. G., and Bauer, S. J. (1992). Solar wind effects on atmosphere evolution at Venus and Mars. *Geophys. Monogr. Ser.* 66, 417–430. doi:10.1029/GM066p0417

Lundin, R., Lammer, H., and Ribas, I. (2007). Planetary magnetic fields and solar forcing: implications for atmospheric evolution. *Space Sci. Res.* 129, 245–278. doi:10.1007/s11214-007-9176-4

Lundin, R., Winningham, D., Barabash, S., Frahm, R. A., Andersson, H., Holmström, M., et al. (2006). Ionospheric plasma acceleration at Mars: ASPERA-3 results. *Icarus* 182, 308–319. doi:10.1016/j.icarus.2005.10.035

Lundin, R., Zakharov, A., Pellinen, R., Barabasj, S. W., Borg, H., Dubinin, E. M., et al. (1990). Aspera/Phobos measurements of the ion outflow from the MARTIAN ionosphere. *Geophys. Res. Lett.* 17, 873–876. doi:10.1029/GL017i006p00873

Lundin, R., Zakharov, A., Pellinen, R., Borg, H., Hultqvist, B., Pissarenko, N., et al. (1989). First measurements of the ionospheric plasma escape from Mars. *Nature* 341, 609–612. doi:10.1038/341609a0

Mazelle, C., and Neubauer, F. M. (1993). Discrete wave packets at the proton cyclotron frequency at comet P/Halley. *Geophys. Res. Lett.* 20, 153–156. doi:10.1029/92GL02613

Mazelle, C., Winterhalter, D., Sauer, K., Trotignon, J. G., Acuña, M. H., Baumgärtel, K., et al. (2004). Bow shock and upstream phenomena at Mars. *Space Sci. Rev.* 111, 115–181. doi:10.1023/B:SPAC.0000032717.98679.d0

McClintock, W. E., Bradley, E. T., Vervack, R. J., Killen, R. M., Sprague, A. L., Izenberg, N. R., et al. (2008). Mercury's exosphere: observations during MESSENGER's first Mercury flyby. *Science* 321, 92–94. doi:10.1126/science.1159467

McClintock, W. E., Vervack, R. J., Bradley, E. T., Killen, R. M., Mouawad, N., Sprague, A. L., et al. (2009). MESSENGER observations of Mercury's exosphere: detection of magnesium and distribution of constituents. *Science* 324, 610–613. doi:10.1126/science.1172525

McComas, D. J., Nordholt, J. E., Bertelier, J.-J., Illiano, J.-M., and Young, D. T. (2010). "The cassini ion mass spectrometer," in *Measurement techniques in space plasmas - particles*. Editors R. F. Pfaff, J. E. Borovsky, and D. T. Young (Washington, USA: AGU), 187–193. doi:10.1029/GM102p018

Means, J. D. (1972). Use of the three-dimensional covariance matrix in analyzing the polarization properties of plane waves. *J. Geophys. Res.* 77, 5551–5559. doi:10.1029/JA077i028p05551

Modolo, R., Chanteur, G. M., Dubinin, E., and Matthews, A. P. (2005). Influence of the solar EUV flux on the Martian plasma environment. *Ann. Geophys.* 23, 433–444. doi:10.5194/angeo-23-433-2005

Nagy, A. F., and Cravens, T. E. (1988). Hot oxygen atoms in the upper atmospheres of Venus and Mars. *Geophys. Res. Lett.* 15, 433–435. doi:10.1029/GL015i005p00433

Neubauer, F. M., Marschall, H., Pohl, M., Glassmeier, K.-H., Musmann, G., Mariani, F., et al. (1993). First results from the Giotto magnetometer experiment during the P/Grigg-Skjellerup encounter. *Astron. Astrophys.* 268, L5–L8.

Orsini, S., Livi, S. A., Lichtenegger, H., Barabash, S., Milillo, A., De Angelis, E., et al. (2021). SERENA: particle instrument suite for determining the sun-mercury interaction from BepiColombo. *Space Res. Rev.* 217, 11. doi:10.1007/s11214-020-00787-3

Orsini, S., Milillo, A., Lichtenegger, H., Varsani, A., Barabash, S., Livi, S., et al. (2022). Inner southern magnetosphere observation of Mercury via SERENA ion sensors in BepiColombo mission. *Nat. Comm.* 13, 7390. doi:10.1038/s41467-022-34988-x

Owen, T., Maillard, J. P., de Bergh, C., and Lutz, B. L. (1988). Deuterium on Mars: the abundance of HDO and the value of D/H. *Science* 240, 1767–1770. doi:10.1126/science.240.4860.1767

Paxton, L. J. (1985). Pioneer Venus orbiter ultraviolet spectrometer limb observations: analysis and interpretation of the 166- and 156-nm data. *J. Geophys. Res.* 90, 5089–5096. doi:10.1029/JA090iA06p05089

Persson, M., Futaana, Y., Fedorov, A., Nilsson, H., Hamrin, M., and Barabash, S. (2018). H^+/O^+ escape rate ratio in the venus magnetotail and its dependence on the solar cycle. *Geophys. Res. Lett.* 45 (10), 805–811. doi:10.1029/2018GL079454

Persson, M., Futaana, Y., Nilsson, H., Stenberg Wieser, G., Hamrin, M., Fedorov, A., et al. (2019). Heavy ion flows in the upper ionosphere of the venusian north Pole. *J. Geophys. Res.* 124, 4597–4607. doi:10.1029/2018JA026271

Porco, C. C., Helfenstein, P., Thomas, P. C., Ingersoll, A. P., Wisdom, J., West, R., et al. (2006). Cassini observes the active south pole of Enceladus. *Science* 311, 1393–1401. doi:10.1126/science.1123013

Potter, A., and Morgan, T. (1985). Discovery of sodium in the atmosphere of Mercury. *Science* 229, 651–653. doi:10.1126/science.229.4714.651

Potter, A. E., and Morgan, T. H. (1986). Potassium in the atmosphere of Mercury. *Icarus* 67, 336–340. doi:10.1016/0019-1035(86)90113-2

Quémerais, E., Koutroumpa, D., Lallement, R., Sandel, B. R., Robidel, R., Chaufray, J.-Y., et al. (2023). Observation of helium in Mercury's exosphere by PHEBUS on bepi-colombo. *J. Geophys. Res. (Planets)* 128, e2023JE007743. doi:10.1029/2023JE007743

Regoli, L. H., Coates, A. J., Thomsen, M. F., Jones, G. H., Roussos, E., Waite, J. H., et al. (2016). Survey of pickup ion signatures in the vicinity of Titan using CAPS/IMS. *J. Geophys. Res.* 121, 8317–8328. doi:10.1002/2016JA022617

Rodriguez, J. M., Prather, M. J., and McElroy, M. B. (1984). Hydrogen on venus: exospheric distribution and escape. *Planet. Space Sci.* 32, 1235–1255. doi:10.1016/0032-0633(84)90067-9

Rojas Mata, S., Stenberg Wieser, G., Futaana, Y., Bader, A., Persson, M., Fedorov, A., et al. (2022). Proton temperature anisotropies in the venus plasma environment during solar minimum and maximum. *J. Geophys. Res. Space Phys.* 127, e29611. doi:10.1029/2021JA029611

Romanelli, N., Bertucci, C., Gómez, D., Mazelle, C., and Delva, M. (2013). Proton cyclotron waves upstream from Mars: observations from Mars global surveyor. *Planet. Space Sci.* 76, 1–9. doi:10.1016/j.pss.2012.10.011

Romanelli, N., Mazelle, C., Chaufray, J. Y., Meziane, K., Shan, L., Ruhunusiri, S., et al. (2016). Proton cyclotron waves occurrence rate upstream from Mars observed by MAVEN: associated variability of the Martian upper atmosphere. *J. Geophys. Res.* 121 (11), 113–128. doi:10.1002/2016JA023270

Rosenbauer, H., Shutte, N., Apáthy, I., Galeev, A., Gringauz, K., Grünwaldt, H., et al. (1989). Ions of martian origin and plasma sheet in the martian magnetosphere: initial results of the TAUS experiment. *Nature* 341, 612–614. doi:10.1038/341612a0

Russell, C., and Blancocano, X. (2007). Ion-cyclotron wave generation by planetary ion pickup. *J. Atmos. Solar-Terrest. Phys.* 69, 1723–1738. doi:10.1016/j.jastp.2007.02.014

Russell, C. T., Blanco-Cano, X., Wang, Y. L., and Kivelson, M. G. (2003). Ion cyclotron waves at Io: implications for the temporal variation of Io's atmosphere. *Planet. Space Sci.* 51, 937–944. doi:10.1016/j.pss.2003.05.005

Russell, C. T., Childers, D. D., and Coleman, J. P. J. (1971). Ogo 5 observations of upstream waves in the interplanetary medium: discrete wave packets. *J. Geophys. Res.* 76, 845–861. doi:10.1029/JA076i004p00845

Russell, C. T., Luhmann, J. G., Schwingenschuh, K., Riedler, W., and Yeroshenko, Y. (1990). Upstream waves at Mars: Phobos observations. *Geophys. Res. Lett.* 17, 897–900. doi:10.1029/GL017i006p00897

Russell, C. T., Wei, H. Y., Cowee, M. M., Neubauer, F. M., and Dougherty, M. K. (2016). Ion cyclotron waves at Titan. *J. Geophys. Res.* 121, 2095–2103. doi:10.1002/2015JA022293

Samson, J. C., and Olson, J. V. (1980). Some comments on the descriptions of the polarization states of waves. *Geophys. J.* 61, 115–129. doi:10.1111/j.1365-246X.1980.tb04308.x

Scarf, F. L., Fredricks, R. W., Frank, L. A., and Neugebauer, M. (1971). Nonthermal electrons and high-frequency waves in the upstream solar wind, 1. Observations. *J. Geophys. Res.* 76, 5162–5171. doi:10.1029/JA076i022p05162

Schmid, D., Lammer, H., Plaschke, F., Vorburger, A., Erkaev, N. V., Wurz, P., et al. (2022). Magnetic evidence for an extended hydrogen exosphere at Mercury. *J. Geophys. Res. (Planets)* 127, e2022JE007462. doi:10.1029/2022JE007462

Schmid, D., Lammer, H., Weichbold, F., Scherf, M., Varsani, A., Volwerk, M., et al. (2025). First detection of Lithium in Mercury's exosphere. *Nature Communications*. doi:10.1038/s41467-025-61516-4

Schmid, D., Narita, Y., Plaschke, F., Volwerk, M., Nakamura, R., and Baumjohann, W. (2021). Pick up ion cyclotron waves around Mercury. *Geophys. Res. Lett.* 48, e92606. doi:10.1029/2021GL092606

Shan, L., Lu, Q., Wu, M., Gao, X., Huang, C., Zhang, T., et al. (2014). Transmission of large-amplitude ULF waves through a quasi-parallel shock at Venus. *J. Geophys. Res. Space Phys.* 119, 237–245. doi:10.1002/2013JA019396

Shematovich, V. I., Bisikalo, D. V., Barabash, S., and Stenberg, G. (2014). Monte Carlo study of interaction between solar wind plasma and Venusian upper atmosphere. *Sol. Syst. Res.* 48, 317–323. doi:10.1134/S0038094614050049

Simon Wedlund, C., Behar, E., Kallio, E., Nilsson, H., Alho, M., Gunell, H., et al. (2019a). Solar wind charge exchange in cometary atmospheres. II. Analytical model. *Astron. Astrophys.* 630, A36. doi:10.1051/0004-6361/201834874

Simon Wedlund, C., Bodewits, D., Alho, M., Hoekstra, R., Behar, E., Gronoff, G., et al. (2019b). Solar wind charge exchange in cometary atmospheres. I. Charge-changing and ionization cross sections for He and H particles in H_2O. *Astron. Astrophys.* 630, A35. doi:10.1051/0004-6361/201834848

Simon Wedlund, C., Kallio, E., Alho, M., Nilsson, H., Stenberg Wieser, G., Gunell, H., et al. (2016). The atmosphere of comet 67P/Churyumov-Gerasimenko diagnosed by charge-exchanged solar wind alpha particles. *Astron. Astrophys.* 587, A154. doi:10.1051/0004-6361/201527532

Smith, B. A., Soderblom, L. A., Johnson, T. V., Ingersoll, A. P., Collins, S. A., Shoemaker, E. M., et al. (1979). The Jupiter system through the eyes of Voyager 1. *Science* 204, 951–972. doi:10.1126/science.204.4396.951

Smith, E. J., and Tsurutani, B. T. (1983). Saturn's magnetosphere: observations of ion cyclotron waves near the dione L shell. *J. Geophys. Res.* 88, 7831–7836. doi:10.1029/JA088iA10p07831

Sprague, A. L., Hunten, D. M., and Grosse, F. A. (1996). Upper limit for lithium in Mercury's atmosphere. *Icarus* 123, 345–349. doi:10.1006/icar.1996.0163

Takacs, P. Z., Broadfoot, A. L., Smith, G. R., and Kumar, S. (1980). Mariner 10 observations of hydrogen Lyman alpha emission from the venus exosphere: evidence of complex structure. *Planet. Space Sci.* 28, 687–701. doi:10.1016/0032-0633(80)90114-2

Taylor, H. A. J., Mayr, H. G., Niemann, H. B., and Larson, J. (1985). Empirical model of the composition of the Venus ionosphere Repeatable characteristics and key features not modeled. *Adv. Space Res.* 5, 157–163. doi:10.1016/0273-1177(85)90284-4

Teolis, B., Sarantos, M., Schorghofer, N., Jones, B., Grava, C., Mura, A., et al. (2023). Surface exospheric interactions. *Space Sci. Rev.* 219, 4. doi:10.1007/s11214-023-00951-5

Tokar, R. L., Wilson, R. J., Johnson, R. E., Henderson, M. G., Thomsen, M. F., Cowee, M. M., et al. (2008). Cassini detection of water-group pick-up ions in the Enceladus torus. *Geophys. Res. Lett.* 35, L14202. doi:10.1029/2008GL034749

Vervack, R. J., Killen, R. M., McClintock, W. E., Merkel, A. W., Burger, M. H., Cassidy, T. A., et al. (2016). New discoveries from MESSENGER and insights into Mercury's exosphere. *Geophys. Res. Lett.* 43 (11), 11545–11551. doi:10.1002/2016GL071284

Vervack, R. J., McClintock, W. E., Killen, R. M., Sprague, A. L., Anderson, B. J., Burger, M. H., et al. (2010). Mercury's complex exosphere: results from MESSENGER's third flyby. *Science* 329, 672–675. doi:10.1126/science.1188572

Volwerk, M., Khurana, K. K., Roux, J. l., and Coates, A. J. (2010). "Ion pick-up near the icy Galilean satellites,". Pickup ions throughout the heliosphere and beyond, AIP conference proceedings. Editors J. A. le Roux, V. Florinski, and G. P. Zank (Melville, NY, USA: IAP), 1302, 263–269. doi:10.1063/1.3529982

Volwerk, M., Kivelson, M. G., and Khurana, K. K. (2001). Wave activity in Europa's wake: implications for ion pick-up. *J. Geophys. Res.* 106, 26033–26048. doi:10.1029/2000JA000347

Volwerk, M., Kivelson, M. G., Khurana, K. K., and McPherron, R. L. (1999). Probing Ganymede's magnetosphere with field line resonances. *J. Geophys. Res.* 104, 14729–14738. doi:10.1029/1999JA900161

Volwerk, M., Koenders, C., Delva, M., Richter, I., Schwingenschuh, K., Bentley, M. S., et al. (2013a). Ion cyclotron waves during the Rosetta approach phase: a magnetic estimate of cometary outgassing. *Ann. Geophys.* 31, 2201–2206. doi:10.5194/angeo-31-2201-2013

Volwerk, M., Koenders, C., Delva, M., Richter, I., Schwingenschuh, K., Bentley, M. S., et al. (2013b). Corrigendum to 'Ion cyclotron waves during the Rosetta approach phase: a magnetic estimate of cometary outgassing' published in. *Ann. Geophys.* 31, 2201–2206. 2013. *Ann. Geophysicae* 31. doi:10.5194/angeo-31-2213-2013

Warnecke, J., Kivelson, M. G., Khurana, K. K., Huddleston, D. E., and Russell, C. T. (1997). Ion cyclotron waves observed at Galileo's Io encounter: implications for neutral cloud distribution and plasma composition. *Geophys. Res. Lett.* 24, 2139–2142. doi:10.1029/97gl01129

Wasson, J. T., and Kallemeyn, G. W. (1988). Compositions of chondrites. *Philosoph. Trans. R. Soc. Lond. Ser. A* 325, 535–544. doi:10.1098/rsta.1988.0066

Watson, C. C. (1982). The sputter-genration of planetary coronae: Galilean satellites of Jupiter. *Lunar Planet. Sci. Conf. Proc.* 12, 1569–1583.

Webster, C. R., Mahaffy, P. R., Flesch, G. J., Niles, P. B., Jones, J. H., Leshin, L. A., et al. (2013). Isotope ratios of H, C, and O in $CO_2$and H_2O of the martian atmosphere. *Science* 341, 260–263. doi:10.1126/science.1237961

Wei, H. Y., Cowee, M. M., Russell, C. T., and Leinweber, H. K. (2014). Ion cyclotron waves at Mars: occurrence and wave properties. *J. Geophys. Res.* 119, 5244–5258. doi:10.1002/2014JA020067

Wei, H. Y., and Russell, C. T. (2006). Proton cyclotron waves at Mars: exosphere structure and evidence for a fast neutral disk. *Geophys. Res. Lett.* 33, L23103. doi:10.1029/2006GL026244

Wei, H. Y., Russell, C. T., Zhang, T. L., and Blanco-Cano, X. (2011). Comparative study of ion cyclotron waves at Mars, Venus and Earth. *Planet. Space Sci.* 59, 1039–1047. doi:10.1016/j.pss.2010.01.004

Weichbold, F. (2023). Mercury's exospheric composition determined by Ion-Cyclotron Wave Analysis. Master's Thesis. *Space Sciences and Earth from Space*. Graz, Austria: Graz University of Technology, 76.

Weichbold, F., Lammer, H., Schmid, D., Volwerk, M., Hener, J., Varsani, A., et al. (2025). Helium in Mercury's extended exosphere determined by pick-up generated ion cyclotron waves. J. Geophys. Res. *(Planets)* 130, e2024JE008679. doi:10.1029/2024JE008679

Wurz, P., Fatemi, S., Galli, A., Halekas, J., Harada, Y., Jäggi, N., et al. (2022). Particles and photons as drivers for particle release from the surfaces of the moon and Mercury. *Space Sci. Rev.* 218, 10. doi:10.1007/s11214-022-00875-6

Wurz, P., Gamborino, D., Vorburger, A., and Raines, J. M. (2019). Heavy ion composition of Mercury's magnetosphere. *J. Geophys. Res.* 124, 2603–2612. doi:10.1029/2018JA026319

Yumoto, K., and Nakagawa, T. (1986). Hydromagnetic waves near O+ (or H2O+) ion cyclotron frequency observed by sakigake at the closest approach to comet Halley. *Geophys. Res. Lett.* 13, 825–828. doi:10.1029/GL013i008p00825

Zhao, D., Guo, J., Lin, H., Meng, W., He, L., Chen, Y., et al. (2023). Upstream proton cyclotron waves at Mars during the passage of solar wind stream interaction regions. *Astron. Astrophys.* 674, A158. doi:10.1051/0004-6361/202346199